Check for updates

DEVELOPMENTAL NEUROSCIENCE

Chronic exposure to glucocorticoids amplifies inhibitory neuron cell fate during human neurodevelopment in organoids

Leander Dony[1,2,3,4,5], Anthi C. Krontira[1], Lea Kaspar[1,2], Ruhel Ahmad[1], Ilknur Safak Demirel[6], Malgorzata Grochowicz[6], Tim Schäfer[6], Fatema Begum[1], Vincenza Sportelli[1,5], Catarina Raimundo[1], Maik Koedel[1], Marta Labeur[1], Silvia Cappello[5,7,8], Fabian J. Theis[3,4,5,9], Cristiana Cruceanu[1,6]*, Elisabeth B. Binder[1,5,8]*

Copyright © 2025 The Authors, some rights reserved; exclusive licensee American Association for the Advancement of Science. No claim to original U.S. Government Works. Distributed under a Creative Commons Attribution NonCommercial License 4.0 (CC BY-NC).

Disruptions in the tightly regulated process of human brain development have been linked to increased risk for brain and mental illnesses. While the genetic contribution to these diseases is well established, important environmental factors have been less studied at molecular and cellular levels. Here, we used single-cell and cell type–specific techniques to investigate the effect of glucocorticoid (GC) exposure, a mediator of antenatal environmental risk, on gene regulation and lineage specification in unguided human neural organoids. We characterized the transcriptional response to chronic GC exposure during neural differentiation and studied the underlying gene regulatory networks by integrating single-cell transcriptomics with chromatin accessibility data. We found lasting cell type–specific changes that included autism risk genes and several transcription factors associated with neurodevelopment. Chronic GC exposure influenced lineage specification primarily by priming the inhibitory neuron lineage through transcription factors like *PBX3*. We provide evidence for convergence of genetic and environmental risk factors through a common mechanism of altering lineage specification.

INTRODUCTION

Human neurodevelopment is a tightly regulated process starting early in embryogenesis that choreographs cellular proliferation, migration, differentiation, and synaptogenesis. The precise timing and sequence of these events are essential to establish neural circuits that govern cognitive, emotional, and behavioral functions. Deviations from this program have been linked to a spectrum of neurodevelopmental and psychiatric disorders, including autism spectrum disorders (ASDs) and schizophrenia. This is supported by the strong enrichment of genes carrying genetic variants associated with these disorders in molecular and cellular pathways essential for neurodevelopment (*1*–*3*). Modeling the effects of associated deleterious variants in transgenic animals and induced pluripotent stem cell–derived model systems supports their impact on neurodevelopment (*4*, *5*).

While these disorders have a large genetic component, with heritability estimates from twin studies around 75% (*6*), environmental risk factors during pregnancy such as chemicals (*7*), infections (*8*), perinatal complications (*9*, *10*), and exposure to glucocorticoids (GCs) (*11*) have also been implicated in increasing disease risk by affecting neurodevelopment. With this work, we aimed to elucidate the contribution of one such prenatal environmental factor, GCs, which are steroid hormones with critical endogenous roles in normal brain development and important pharmacological applications during pregnancy (*11*). Activation of the GC receptor in the developing brain plays an essential role in neurogenesis, neuronal migration, synaptogenesis, and modulation of neuronal plasticity (*11*). Perturbations in GC signaling during critical periods of brain development have been proposed to lead to long-lasting alterations in brain structure and function, potentially contributing to the pathogenesis of psychiatric disorders (*12*–*14*). Animal models and human studies have provided compelling evidence for substantial effects of GC excess during gestation on cognitive and emotional development. During pregnancies at risk of premature delivery, synthetic GCs such as betamethasone and dexamethasone (Dex) are routinely used to promote lung maturation in the unborn child. Large epidemiological studies have linked such antenatal exposure to synthetic GCs to altered risk for childhood mental and behavioral problems (*15*–*17*). An increase in risk is observed mainly when synthetic GCs are administered later in pregnancy, while the opposite was observed for extremely preterm babies born at less than 28 weeks of gestation (*18*, *19*). Given that more than 10% of babies (~13 million) were born prematurely worldwide in 2020, this is a sizable environmental risk factor for brain development (*20*).

Despite the strong evidence for harmful effects from epidemiological studies, there is limited evidence on the underlying molecular and cellular mechanisms (*11*, *21*). Using human neural organoids as models of early brain development, we could recently show that GCs elicit cell type–specific transcriptional responses and that there is a highly significant enrichment of genes associated with neurodevelopmental delay, ASD, and more common psychiatric disorders among those regulated by GCs, especially in neurons (*22*). Furthermore, we showed that GCs, through dysregulation of key transcription factors (TFs) in neural progenitors, can have lasting effects on

[1]Department Genes and Environment, Max Planck Institute of Psychiatry, 80804 Munich, Germany. [2]International Max Planck Research School for Translational Psychiatry (IMPRS-TP), 80804 Munich, Germany. [3]Institute of Computational Biology, Computational Health Center, Helmholtz Munich, 85764 Neuherberg, Germany. [4]TUM School of Life Sciences Weihenstephan, Technical University of Munich, 85354 Freising, Germany. [5]German Center for Mental Health (DZPG), partner site Munich, Munich, Germany. [6]Department of Physiology and Pharmacology, Karolinska Institutet, Stockholm, Sweden. [7]Physiological Genomics, Biomedical Center (BMC), LMU Munich Faculty of Medicine, 82152 Planegg-Martinsried, Germany. [8]Max Planck Institute of Psychiatry, 80804 Munich, Germany. [9]TUM School of Computation, Information and Technology, Technical University of Munich, 85748 Garching bei München, Germany.
*Corresponding author. Email: binder@psych.mpg.de (E.B.B.); cristiana.cruceanu@ki.se (C.C.)

Downloaded from https://www.science.org at Helmholtz Zentrum Mnchen - Zentralbibliothek on April 09, 2025

corticogenesis, which in turn are associated with positive outcomes in the development of cognition processes (*23*). This suggests a convergence of the molecular pathways underpinning genetic and environmental risk factors for neuropsychiatric and behavioral phenotypes.

The advent of human neural organoids now allows us to better link risk or resilience genes for neurodevelopmental disorders (NDDs) to molecular and cellular mechanisms. Data from cerebral organoids derived from induced pluripotent stem cells from patients with idiopathic ASD or carrying rare coding or copy number variants associated with ASD suggest that cell fate specification is altered by risk genes carrying deleterious mutations, with particular support for alterations in the proportions of excitatory versus inhibitory neuronal lineages or dorsal versus ventral arealization (*24*–*28*). These findings are further supported by results from a CRISPR–human organoids–single-cell RNA sequencing (CHOOSE) system, in which 36 high-risk ASD genes were perturbed. These risk genes were selected among other autism risk genes for their relation to transcriptional regulation, and their perturbation uncovered consistent effects on cell fate determination, mainly shifting the dorsal-to-ventral ratio at different levels (*29*).

With this article, we aim to address whether the convergence of risk genes for neuropsychiatric and neurodevelopmental disorders and genes regulated by antenatal exposure to GC, an environmental risk factor for childhood mental and neurodevelopmental disorders, extends beyond the molecular context to alteration of cell fate specification. For this, we exposed unguided and regionalized neural organoids to a chronic administration of the synthetic GC Dex, a drug that is commonly used clinically in pregnancies at risk of premature labor. We assessed cell type–specific responses with single-cell RNA sequencing (scRNA-seq) and single-cell assay for transposase-accessible chromatin using sequencing (scATAC-seq) analyses directly after the chronic administration and following a washout period. Our work advances the current knowledge by demonstrating a convergent impact of environmental and genetic risk factors for mental and neurodevelopmental disorders on cell fate determination in the developing brain.

RESULTS

Chronic GC exposure in neural organoids does not induce significant metabolic stress in cells

To elucidate the effects of GCs on neurodevelopmental processes, we designed an exposure paradigm in unguided neural organoids. We collected 70-day-old organoids, continuously exposed to GCs for 10 days, starting at day 60 (Chr condition) and the matching vehicle control organoids (Veh condition), allowing us to measure the immediate transcriptional effects of chronic GC exposure. Furthermore, we were interested in understanding which transcriptional changes lasted for an extended period in organoids. For this, we collected organoids from the Veh and Chr conditions after an additional 20 days under standard culture conditions at day 90 (Veh-Veh and Chr-Veh conditions, respectively). Last, we wanted to understand the differences between the transcriptional effects of chronic and acute exposure. Therefore, we obtained samples at day 90, exposed to an additional 12-hour acute GC treatment before collection (Veh-Acu and Chr-Acu conditions). We duplicated all analyses using organoids derived from two human induced pluripotent stem cell (hiPSC) lines, Line 409b2 and Line FOK4, with four replicates in each of the six experimental conditions (Fig. 1).

We generated scRNA-seq data from all conditions. We combined these data to determine the cell type composition in organoids derived from the two iPSC lines. Basing our analysis on known marker genes of cell types in the developing human brain, we were able to identify and label eight of the nine cell clusters in each of the lines (Fig. 2A and fig. S1A): Radial Glia (RG) (*GPM6B*, *SOX2*), neural progenitor cells (NPCs) expressing cell cycle markers (Cycling) (*TOP2A*, *MKI67*), Intermediate Progenitors (IP) (*EOMES*, *PAX6*), Excitatory Neurons (Ex. Neurons) (*SLC17A6*, *STMN2*), Inhibitory Neurons (Inh. Neurons) (*GAD1*, *GAD2*, *SLC32A1*, *STMN2*), a population of unspecified neurons expressing the G protein regulator gene *RGS5* (RGS5 Neurons) (*RGS5*, *LINC00682*, *STMN2*), immature Choroid Plexus cells (Imm. ChP) (*RSPO3*, *TPBG*), as well as more mature cells of the Choroid Plexus (ChP) (*TTR*, *HTR2C*, *CLIC6*).

We also identified a cluster of cells in the datasets from both lines, which did not express any clear combination of known marker genes. We identified many of these cells as metabolically challenged by scoring previously suggested pathways specific for nonviable cells in organoids (Fig. 2B) (*30*). We identified 12% of all cells as nonviable in both datasets (4304 cells in Line 409b2 data and 3559 cells in Line FOK4 data). In both cell lines, we found the highest fraction of nonviable cells in the Unknown cluster (74% of cells in Line 409b2 and 41% in Line FOK4), followed by the RGS5 Neurons cluster (54% of cells in Line 409b2 and 15% in Line FOK4). Line 409b2 also had a substantial fraction of IP and Imm. ChP cells identified as nonviable cells (26% and 20%, respectively). For all other cell types, only small fractions of around 10% or less were identified (fig. S1B). We removed all cells identified as nonviable from the datasets. Following removal, the remaining cells of the Unknown cluster still showed low marker gene expression (maximum scanpy marker score Line 409b2: 6; Line FOK4: 38) compared to the rest of the clusters (mean maximum scanpy marker score Line 409b2: 131; Line FOK4: 104). Additionally, the top 10 marker genes of the remaining Unknown cells included several genes involved in cellular stress response, glycolysis, hypoxia, or metabolism in general (fig. S1C). Examples include *NEAT1* (*31*), *MALAT1* (*32*), *CDKN1A* (*33*), *CSKMT* (*34*), and *DDIT3* (*35*). We consequently removed the remaining cells of the Unknown cluster from the dataset. We compared pairwise viability scores between chronically GC-exposed samples and the respective control samples at days 70 and 90 for the different conditions and found no significant difference after removing the nonviable cells (Fig. 2C). This was also true when grouping the chronically treated samples with washout or washout and restimulation (Chr-Veh + Chr-Acu against Veh-Veh + Veh-Acu). The only significant decrease [false discovery rate (FDR)–corrected P value = 0.04] in viability was observed in Line 409b2 when grouping the day 90 samples by acute treatment (Veh-Acu + Chr-Acu against Veh-Veh + Chr-Veh). This was not seen in Line FOK4. Together, these findings support that differential gene expression analyses for the chronic treatment and the majority of the washout conditions, the main focus of this study, are likely not confounded by differences in cell viability after filtering. Removing all nonviable cells from the datasets clarified the relationships of developmentally related cell types in the low-dimensional embeddings (Fig. 2D, top).

Consistent with our previous study (*22*), GC treatment was not a major source of variation during cell cluster definition, where cells were separated mainly by their cell identity in the low-dimensional data representation (Fig. 2D, middle). Furthermore, the expression of the GC receptor gene *NR3C1* was uniform across most cell types

Downloaded from https://www.science.org at Helmholtz Zentrum Mnchen - Zentralbibliothek on April 09, 2025

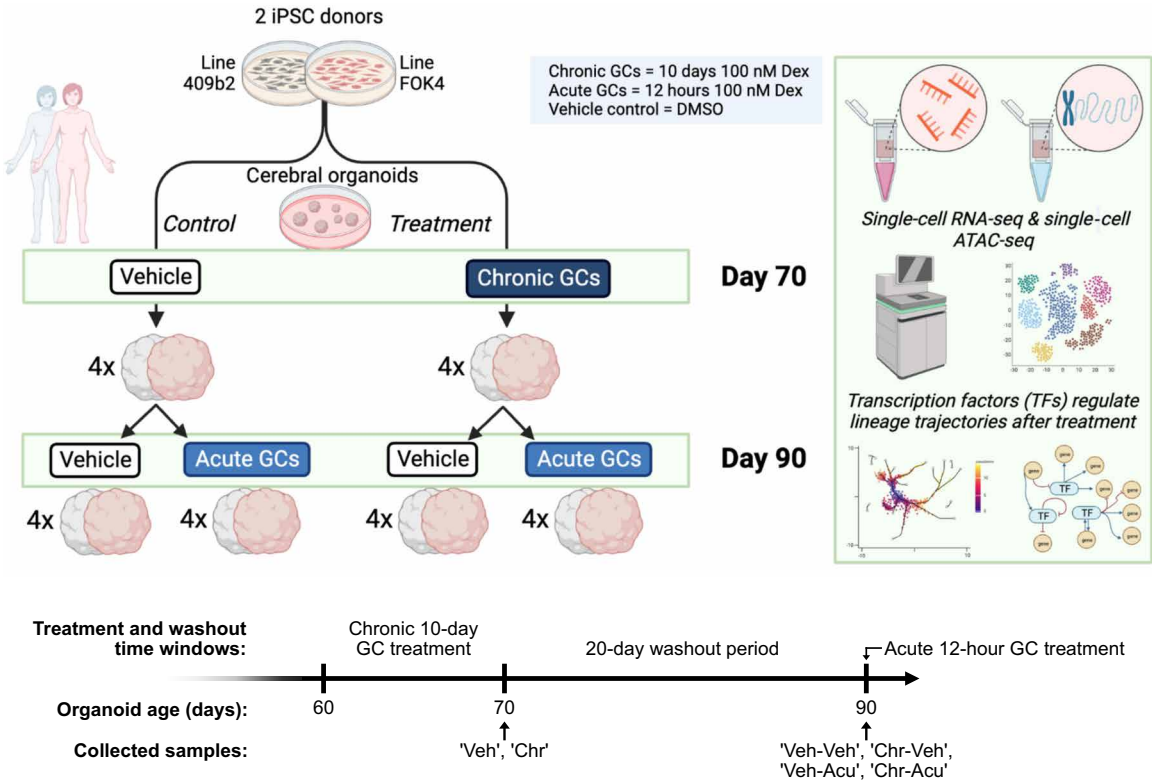

Fig. 1. Overview of experimental setup and design. We designed six treatment conditions duplicated in organoids derived from two cell lines. We replicated each of these 12 conditions using four samples. We collected two treatment conditions at day 70: Veh (exposed to the treatment vehicle DMSO for 10 days starting from day 60) and Chr (exposed to the GC Dex for 10 days starting from day 60). We derived the four additional treatment conditions collected at day 90 from the day 70 conditions with sustained culturing in regular medium conditions for a further 20 days (washout period). The two conditions derived from the Veh condition were Veh-Veh and Veh-Acu, with an additional 12-hour acute GC exposure applied. Analogously, the two day-90 conditions derived from the Chr condition were Chr-Veh and Chr-Acu, with an additional 12-hour acute GC exposure applied. Parts of the figure were created with BioRender.com.

but less pronounced toward the mature end of the neuronal lineage, as described previously (*22*) (Fig. 2D, bottom). The fraction of *NR3C1*-expressing cells did not significantly differ between cell lines (fig. S1D). We did observe differences in *NR3C1* expression levels between lines within specific cell types but not consistently occurring in the same direction (fig. S1E). In addition, *NR3C1* expression levels did not systematically vary with treatment conditions. The fraction of *NR3C1*-expressing cells showed a significantly stronger correlation with *NR3C1* target gene expression than *NR3C1* expression levels themselves (fig. S1F), likely making the former measure more relevant for GC response.

To characterize the regional identity of inhibitory and excitatory neurons in our dataset, we projected them onto our recently published Human Brain Organoid Cell Atlas (HNOCA) (*36*). The neuron subtypes projected to the nontelencephalic inhibitory and excitatory neuronal clusters in HNOCA, while the RG cells projected primarily to nontelencephalic NPCs. Organoids derived from Line 409b2 additionally contained early cells of the glial lineage, whereas organoids derived from Line FOK4 contained a more pronounced lineage of the choroid plexus. Within the neuronal lineage, cells from both lines mapped to similar cell types in HNOCA (fig. S1G), suggesting that organoids from both cell lines contained matching neuronal cells. The expression of regional population markers across the assigned cell types confirmed the nontelencephalic identity of the progenitor and neuron clusters, with a variety of regional markers of the diencephalon, mesencephalon, and rhombencephalon being expressed to various degrees (fig. S1H).

Transcriptional response following chronic GC treatment in organoids includes key neurodevelopmental genes

Next, we sought to identify the transcriptomic and gene regulatory responses to our different GC treatment regimens. We harmonized results across the two iPSC donor backgrounds to ensure robustness in our identified differentially expressed (DE) genes. Specifically, we only deemed a gene as DE if it was significantly regulated at an FDR smaller than 0.1 with an agreeing direction of expression fold change in organoids derived from both cell lines (fig. S2A). This approach reduced the number of DE genes while increasing the robustness of downstream analyses.

This approach identified 803 consensus DE genes across six cell types (RG, Cycling, Inh. Neurons, Ex. Neurons, Imm. ChP, and ChP) (Fig. 3C). IP and RGS5 Neurons did not yield significant DE genes, likely due to power issues caused by smaller cell numbers in these groups or perhaps less convergence of cells within this identified cell type across the temporal differentiation timeline.

Among the top consensus DE genes by fold change were *NNAT*, a gene associated with early neurodevelopment and ion channel control (*37*) [mean $\log_2$ fold change ($\log_2$FC) RG = 0.56]; *MAB21L1*,

Downloaded from https://www.science.org at Helmholtz Zentrum Mnchen - Zentralbibliothek on April 09, 2025

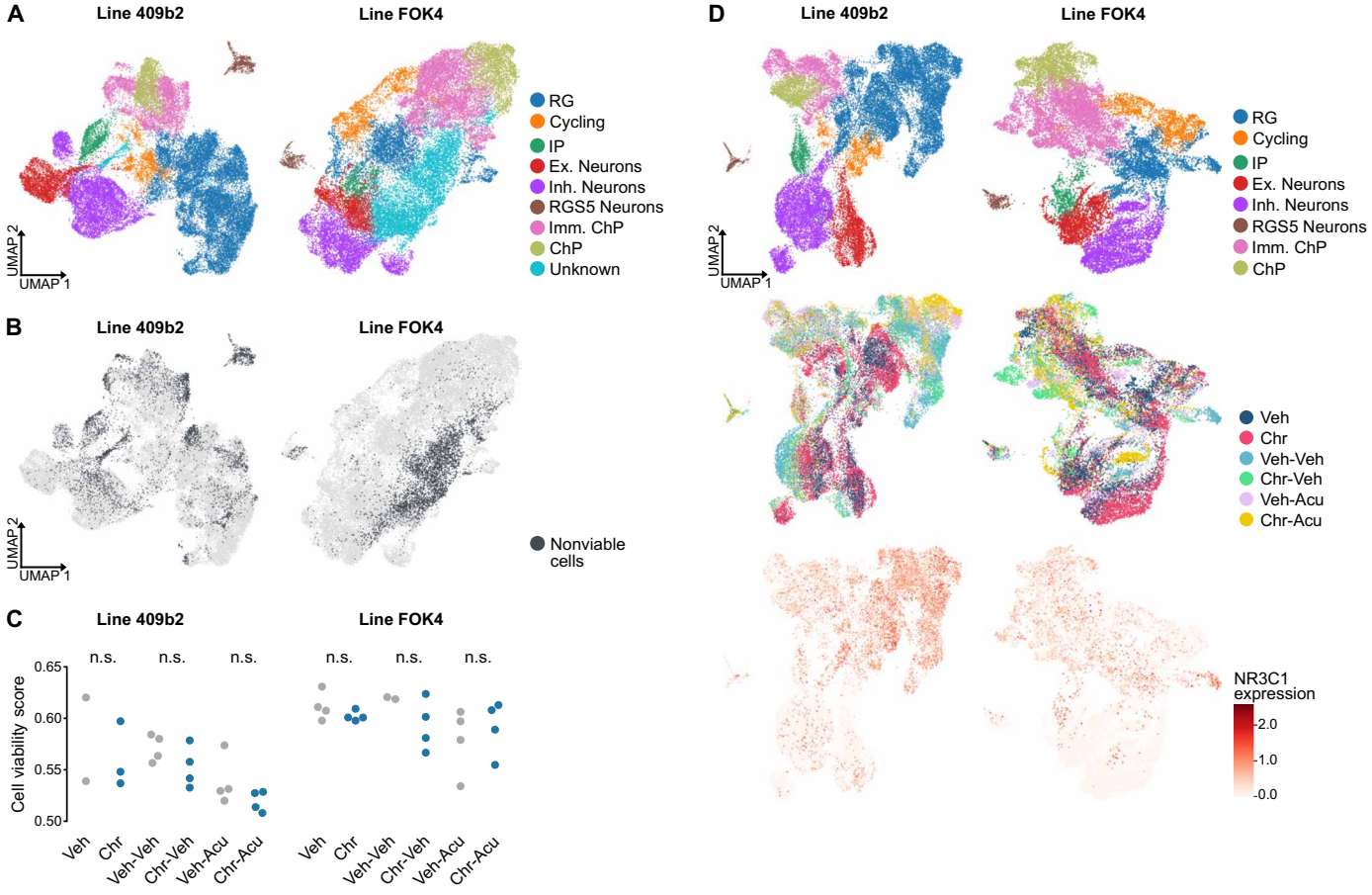

Fig. 2. Chronic GC exposure in neural organoids does not induce significant metabolic stress in cells. (**A**) Cell types on UMAP embedding for Line 409b2 and Line FOK4. Each cell type was identified in both datasets. (**B**) Localization of nonviable cells (charcoal) in the UMAP embedding for Line 409b2 and Line FOK4 organoids. The "Unknown" cluster is primarily made up of nonviable cells (74% in Line 409b2 and 41% in Line FOK4), suggesting that these cells and the entire cluster should be removed. (**C**) Swarm plots, showing no significant difference in mean viability score between control (gray) and treated (blue) samples following nonviable cell removal using an unpaired *t* test. Each dot represents a sample from the indicated treatment condition. (**D**) Top: UMAP embedding colored by cell type for Line 409b2 and Line FOK4 following nonviable cell removal. Middle: UMAP embedding colored by treatment conditions. Bottom: *NR3C1* (GC receptor) gene expression.

associated with cerebellum development (*38*) (mean $\log_2$FC Excitatory Neurons = 0.31); *NEUROD2*, a gene associated with neurodevelopment, ASD, and intellectual disability (*39*) (mean $\log_2$FC Inhibitory Neurons = −0.33); and the transcriptional regulators *ID3* (mean $\log_2$FC in Imm. ChP = 0.46) and *ID2* (mean $\log_2$FC in Imm. ChP and RG = 0.41 and 0.52, respectively). In addition to *NEUROD2*, we identified several additional TFs closely associated with developmental processes as DE in various clusters. Examples include *SOX2*, *HDAC2*, *TCF7L2*, *PBX3*, and *YBX1*. We found that one of these TFs, *YBX1*, was DE in a total of five cell types. Other examples of genes that were DE in five clusters included *DLK1* [a regulator of hippocampal neurogenesis (*40*)] and *MARCKSL1* [associated with neural tube defects and regeneration (*41*)] (Fig. 3C). We next performed pathway enrichment using the Gene Ontology Biological Process (GO-BP) set. This analysis identified enrichment for terms associated with neurodevelopment in the clusters with the most consensus DE genes. These included "axonogenesis," "negative regulation of nervous system development" (RG); "axon development," "substantia nigra development" (Excitatory Neurons); and "cranial nerve development," "regulation of neuron differentiation" (Inhibitory Neurons) (table S2). However, the terms most significantly enriched did not converge on specific neuronal pathways. They were generally associated with cell cycle regulation and intracellular transport in Excitatory Neurons and regulation of gene expression in RG and Inhibitory Neurons (Fig. 3D).

In addition to the TFs mentioned to be regulated above, we also found 72 ASD risk genes from the SFARI Gene database (*42*) DE. Examples include *FABP5* (mean $\log_2$FC RG = −0.37), *ARF3* (mean $\log_2$FC Excitatory Neurons = −0.12), and *BCL11A* (mean $\log_2$FC Inhibitory Neurons = 0.22). When comparing the DE effect directly following chronic GC exposure with the lasting DE effect after the washout period at day 90 (table S3), we observed that 13% of the immediate transcriptomic effects showed persistent, stringent DE after the washout. The nonoverlapping DE genes either are no longer captured after the washout due to differences in sample sizes between the comparisons or are indeed specific to a more short-lived response to GC exposure. Alternatively, given the relatively high number of TFs DE at day 70, these DE effects could have been translated to downstream transcriptional effects, explaining the high fraction (76%) of newly regulated DE genes

Downloaded from https://www.science.org at Helmholtz Zentrum Muchen - Zentralbibliothek on April 09, 2025

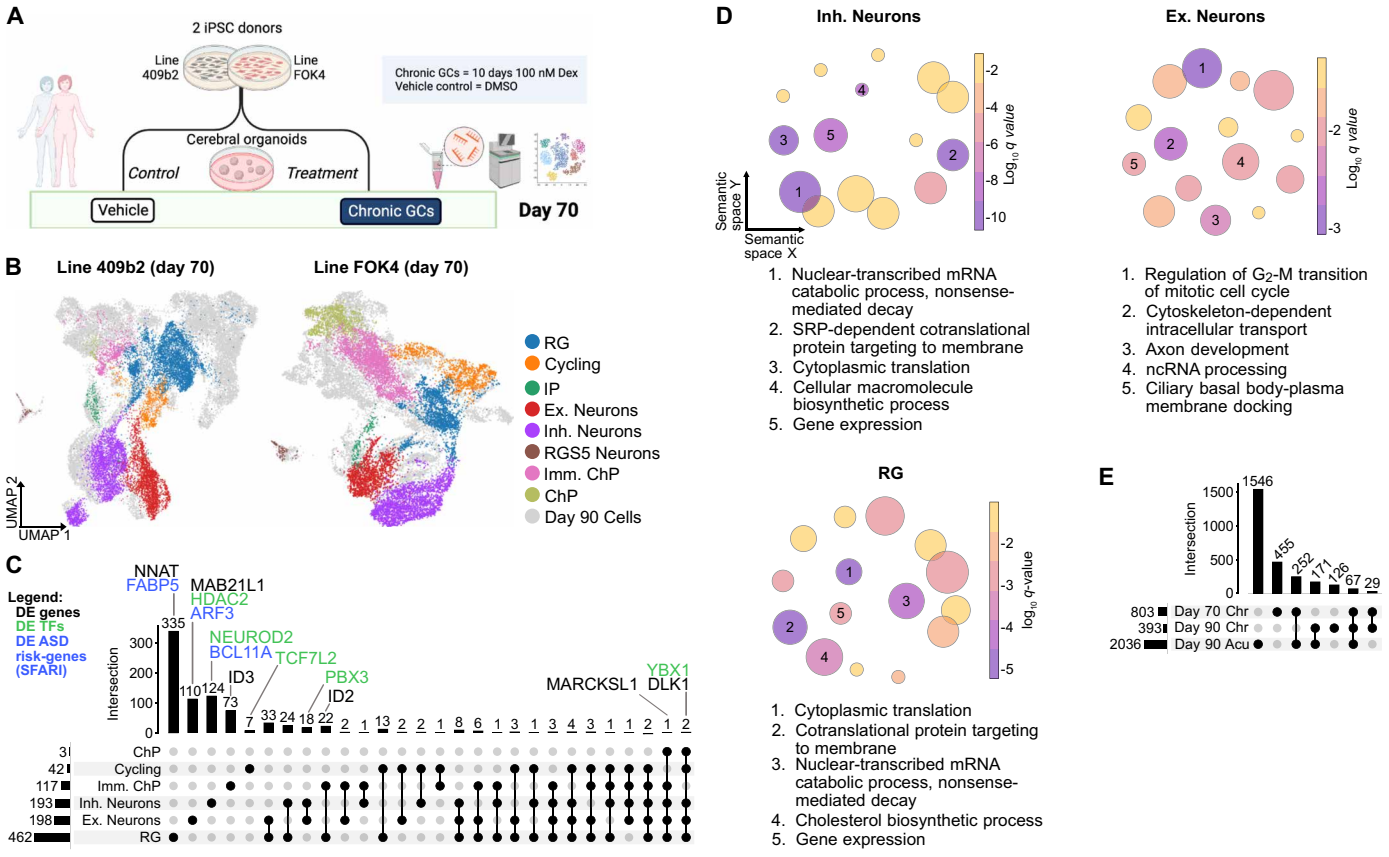

Fig. 3. Transcriptional response following chronic GC treatment in organoids includes key neurodevelopmental genes. (**A**) Overview of the experimental design for 70-day-old organoids. Created with BioRender.com. (**B**) UMAP embedding for day 70 data of Line 409b2 and Line FOK4 at day 70 colored by cell type. Cells from day 90 samples are shown in gray. All identified cell types are present at this earlier stage. (**C**) Upset plot showing consensus DE results per cell type and the number of unique and shared consensus DE genes. Selected genes are highlighted, ASD risk genes from the SFARI Gene database (*42*) are shown in blue, and further TFs are shown in green. (**D**) Grouped semantic space representation of the GO-BP enrichment results for the three cell types with the most detected DE genes. The size of the circles corresponds to the number of terms in the cluster; their color corresponds to the $\log_{10}(q$ value) of the representative term for each cluster. The integers within the circles enumerate the five most significant clusters, and their representative term is written out in the legend below each plot. (**E**) Upset plot showing DE results aggregated across all cell types for the effect of chronic GC exposure directly following the treatment (Day 70 Chr), the effect of chronic GC exposure after a 20-day washout period (Day 90 Chr), and the effect of acute GC exposure in 90-day-old organoids (Day 90 Acu).

following the washout period. Interestingly, 61% of the genes regulated after chronic exposure and washout in 90-day-old organoids overlapped with the genes from the 12-hour acute stimulation at day 90 (table S4). Furthermore, in each cell type with overlapping genes, the directionality of the DE effect was aligned for over 90% of the shared genes. This shows that more than half of the lasting transcriptomic effects after chronic GC exposure were shared with the response to acute GC exposure in 90-day-old organoids, supporting that the lasting effects are closely related to GC activity even after the 20-day washout phase. The overlap with the acute effect was prominent but reduced (40%) in the DE day 70 genes (Fig. 3E), probably due to differences in neurodevelopmental age. Within each cell type in the low-dimensional embedding, cells were separated by organoid age, emphasizing their transcriptomic differences (fig. S2C). We found that 12% of the genes responsive to an acute GC exposure at day 90 had a significantly different response to this exposure based on the organoid's history of chronic treatment, again supporting a lasting effect of the chronic GC exposure (table S5).

GC exposure induces priming of the inhibitory neuron lineage in neural organoids

Having observed a DE effect in genes associated with neurodevelopment directly following treatment, particularly in a subset of high-risk genes for ASD involved in priming neuronal lineage fate (*29*), we next focused on investigating the impact of exposure to GCs on neural fate decisions within our organoid system. For this, we defined three lineage endpoints in our single-cell transcriptome data: Excitatory Neurons, Inhibitory Neurons, and Choroid Plexus (Fig. 4A). As a next step, we computed the lineage probability of every cell for each lineage endpoint along a pseudotime trajectory. For all lineage trajectories, we observed a continuous increase of lineage probability along the trajectories seen in the two-dimensional (2D) embeddings originating from early (RG) cells and reaching maximum lineage probability at the respective lineage endpoint (Fig. 4B). Given our particular interest in neuronal lineage determination and because only a few genes were DE in the ChP-related cell types, we focused on the excitatory and inhibitory neuron lineage endpoints. To account for any potential bias in organoid derivation

Downloaded from https://www.science.org at Helmholtz Zentrum Muenchen - Zentralbibliothek on April 09, 2025

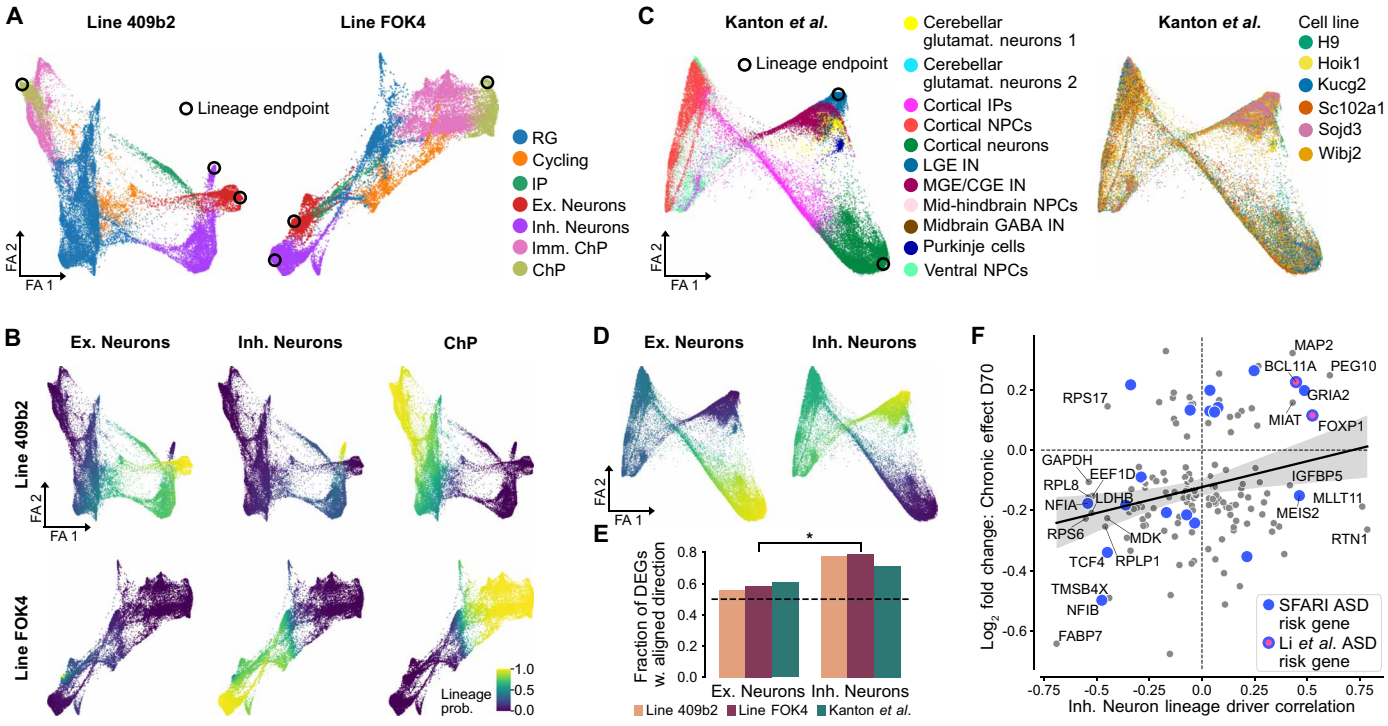

Fig. 4. TF regulation causes priming of the inhibitory neuron lineage in neural organoids. (**A**) Force-directed graph embedding of organoid data from both cell lines (without the RGS5 Neurons cluster) colored by cell type. Lineage endpoints are labeled with black circles. FA, force-directed graph embedding. (**B**) Computed lineage probabilities per cell for the three lineage endpoints in the two datasets. (**C**) Force-directed graph layout of validation data (published 70-day-old organoid data derived from six additional cell lines) (*43*). Colored by cell type (left) and cell line (right). Lineage endpoints are labeled with black circles. CGE, caudal ganglionic eminence; MGE, medial ganglionic eminence; LGE, lateral ganglionic eminence; IN, interneuron; glutamat., glutamatergic; IPs, intermediate progenitors; NPCs, neural progenitor cells. (**D**) Computed lineage probabilities per cell for the two neuronal lineage endpoints visualized on the force-directed graph layout of the validation data from six cell lines. (**E**) Fraction of genes where the directionality of consensus DE effect and driver status was aligned out of all genes both significantly DE (consensus DE genes from Line 409b2 and Line FOK4 data) and in the top 500 significant driver genes (recomputed for each of the three datasets). The dashed line indicates the fraction expected by chance (0.5). Statistical significance was computed using a paired *t* test. (**F**) Magnitude of driver gene correlation with the inhibitory neuron lineage in the validation data (*43*) versus $\log_2$FC of consensus DE effect measured in our two cell lines. Genes with the highest lineage correlation are labeled by name, ASD risk genes from the SFARI Gene database (*42*) are marked in blue, and genes associated with high risk for ASD in the Li *et al.* publication (*29*) are marked in blue with a magenta core.

specific to our experiments, we validated the lineage probabilities in an independently published dataset containing organoid data from six additional iPSC donor backgrounds (*43*). For this, we reprocessed the scRNA-seq data from 70-day-old organoids published by Kanton *et al.* (*43*) (Fig. 4C) and analyzed it with the same lineage inference approach used for our data. We observed similar trends in lineage determination across pseudotime with clear trajectories toward inhibitory and excitatory neurons (Fig. 4D).

Next, we sought to identify genes that are strong drivers of lineage specification. One way of defining a driver gene for a lineage is a strong correlation of the gene's expression level with the computed lineage probability for a specific lineage endpoint (*44*). To quantify the association of the observed DE effect following GC exposure with the different lineages, we computed driver gene correlation in our two datasets and the validation dataset (eight total iPSC donors) (table S6). Next, we overlapped our consensus DE gene list for each neuronal cell type with the top 500 driver genes of the respective neuronal lineage from each of the three datasets. We used the resulting list of genes to compute the proportion of genes for which the directionality of the DE response aligned with the directionality of driving the lineage. For both neuronal lineages, more than half of all DE genes had an aligned direction of DE effect and expression changes along those lineages, suggesting a possible acceleration in neuronal differentiation following GC exposure. Furthermore, we found a significantly larger alignment of the DE effect with the inhibitory neuron lineage drivers in the three datasets ($P = 0.04$) than with the drivers for the excitatory lineage. This suggested that the overall DE effect correlated to a significantly higher degree with the priming of the inhibitory than excitatory neuron lineage (Fig. 4E). Using the driver gene information from the validation dataset only, we observed a significant positive correlation between driver gene strength for the inhibitory neuron lineage and the direction of the DE effect in the inhibitory cell clusters of our two organoid datasets ($r = 0.25$, $P = 0.002$) with a number of ASD risk genes from the SFARI Gene database among them (Fig. 4F).

GC exposure results in an increased abundance of inhibitory neurons in organoids

Next, we aimed to understand whether the observed priming of differentiation and, specifically, of the inhibitory neuron lineage translated into a measurable shift in cell type identity. We selected *GAD1* as a specific marker gene of the inhibitory neuron lineage across brain regions (Fig. 5A). For both of our unguided organoid datasets, we observed an increased proportion of *GAD1*-positive cells at the

Downloaded from https://www.science.org at Helmholtz Zentrum Muenchen - Zentralbibliothek on April 09, 2025

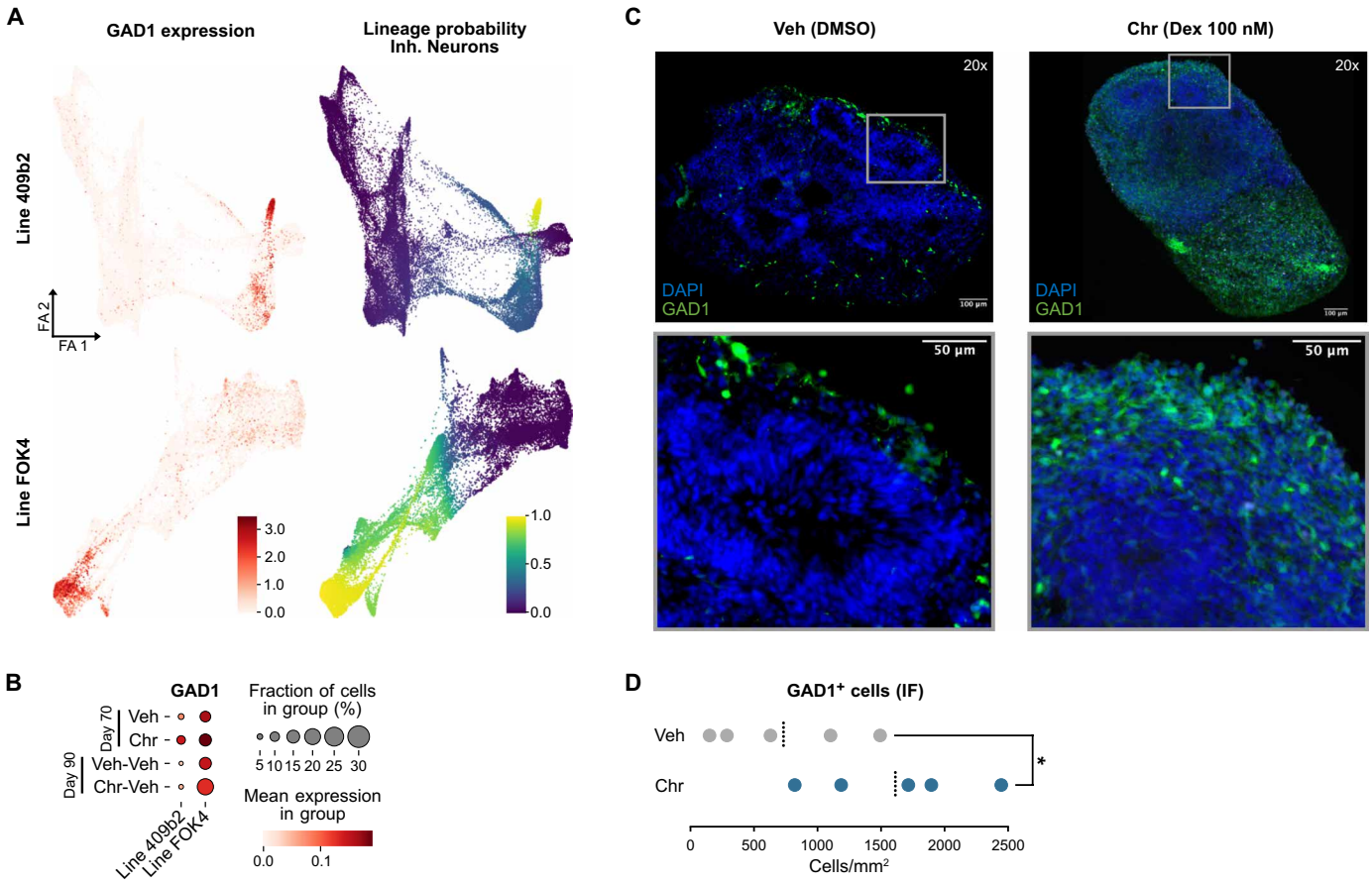

Fig. 5. GC exposure results in an increased abundance of inhibitory neurons in organoids. (**A**) Left: Force-directed graph layout colored by expression of the inhibitory neuron marker *GAD1*. Right: Force-directed graph layout colored by absorption probability per cell for the inhibitory neuron lineage. (**B**) Fraction of *GAD1*-positive cells and mean *GAD1* expression across all cells in Veh Chr, Veh-Veh, and Chr-Veh conditions and organoids from both cell lines. (**C**) Representative images of whole slice ventralized organoids at day 70 in culture, following 10 days of chronic treatment with GCs (100 nM Dex; Chr condition; right) and control (Veh condition; left), show an increased abundance of GAD1$^+$ cells in the treated condition. Images were acquired at ×20 magnification, showing 4′,6-diamidino-2-phenylindole (DAPI) (blue) and GAD1 (green). Lower panel: Zoomed-in insets. (**D**) Cell counting quantification of GAD1$^+$ cells across entire organoid tissue slices ($n = 5$ per condition) and graphically represented as cells/mm^2. Means per condition are indicated as a dotted black line. Statistical significance was computed using an unpaired *t* test. IF, immunofluorescence.

RNA level after exposure to GCs [1.7-fold increase in Line 409b2 (5.2 to 8.7%); 1.2-fold increase in Line FOK4 (11.6 to 13.8%)] (Fig. 5B). The increase in the number of inhibitory neurons was also supported by differential abundance testing (*45*) results. Specifically, we observed a positive log-fold change for the inhibitory neurons following GC exposure in both cell lines, with statistical significance reached in Line FOK4 (fig. S3A). While statistical significance was not reached in Line 409b2, we still observed a markedly larger abundance of cells from the treatment (Chr) condition in the subset of inhibitory neurons with high *GAD1* expression (fig. S3B). The lack of statistical significance in Line 409b2 hence likely arose from a reduced number of replicates for the relevant conditions after quality control (QC) filtering in this cell line. To confirm that the increase in *GAD1*$^+$ cells was not just a result of an increased number of neurons present in GC-exposed organoids, we computed the inhibitory-to-excitatory neuron ratio using *GAD1* and *SLC17A6* as markers for the two groups, respectively. The ratio consistently increased after GC exposure in both datasets [0.52 (Veh) to 0.86 (Chr) in Line 409b2; 2.34 (Veh) to 2.94 (Chr) in Line FOK4].

To understand whether these differences would translate to a more physiological tissue context for inhibitory neuron development, we performed a comparable exposure paradigm in regionalized ventral and dorsal organoids. We obtained these stainings in a new experiment using a CRISPR-Cas9–edited version of Line 409b2 organoids expressing green fluorescent protein (GFP)–tagged GAD1 protein. Guiding differentiation with ventralization factors allowed for a more abundant representation of inhibitory neurons and their differentiation pathways (fig. S3, C to E) (*46*). Our RNA-level results were validated with tissue-level protein expression where more GAD1 signal was apparent in treated organoids (Fig. 5C). Chronic exposure to GCs led to a significant 2.27-fold increase in GAD1$^+$ cells ($P = 0.048$; Fig. 5D and table S7). We replicated this finding in an independent staining experiment (fold change = 2.11; $P = 0.0043$) (table S7). To explore the inhibitory-versus-noninhibitory or excitatory neuron ratio at the protein level, we used costaining with postmitotic neuronal protein NeuN, with or without GAD1. There was no significant difference in NeuN$^+$GAD1$^-$ noninhibitory neurons following GC treatment in dorsalized organoids, but a 3.9-fold significant decrease in ventralized organoids

Downloaded from https://www.science.org at Helmholtz Zentrum Mnchen - Zentralbibliothek on April 09, 2025

(post hoc $P = 0.0014$) (fig. S3F). We also replicated the GAD1$^+$ increase in ventral organoids (fold change = 2.04, post hoc $P = 0.0004$) in this separate experiment (fig. S3G). These data suggest that non-inhibitory neurons (primarily excitatory) are likely decreased at the expense of inhibitory neurons following GC overexposure, but only in tissue committed toward a ventral fate.

Following the 20-day washout period, we still observed an increased number of *GAD1*$^+$ cells in 90-day-old GC-exposed organoids at the RNA level [1.2-fold increase in Line 409b2 (3.4 to 3.9%); 1.5-fold increase in Line FOK4 (13.5 to 20.1%)] (Fig. 5B), while the inhibitory-to-excitatory neuron ratio using *GAD1* and *SLC17A6* as markers at day 90 was not consistent across our two datasets [1.54 (Veh) to 1.15 (Chr) in Line 409b2; 5.29 (Veh) to 6.30 (Chr) in Line FOK4]. In summary, we have observed priming of the inhibitory neuron lineage following GC exposure in our organoid system, resulting in more *GAD1*$^+$ cells at the RNA and protein level in independent experiments, in both unguided and ventralized organoids.

PBX3 regulation through chronic GC exposure supports inhibitory neuron priming

We next set out to study the mechanisms underlying priming of the inhibitory neuron lineage by identifying the lineage-driving TFs with the strongest expression changes following GC exposure in our model system. We identified 15 TFs that had an aligned direction of $\log_2$FC (in inhibitory neurons following GC exposure) and driver correlation (with the inhibitory neuron lineage in the validation data) (Fig. 6A). We hypothesized that a TF that plays a central role in the lineage priming would not only itself be DE after GC exposure but would also have a significant number of its target genes DE. Across all our DE genes and all cell types, we identified 18 TFs that met these criteria: *BCL6*, *EGR1*, *ID2*, *ID3*, *ID4*, *NEUROD1*,

Downloaded from https://www.science.org at Helmholtz Zentrum Mnchen - Zentralbibliothek on April 09, 2025

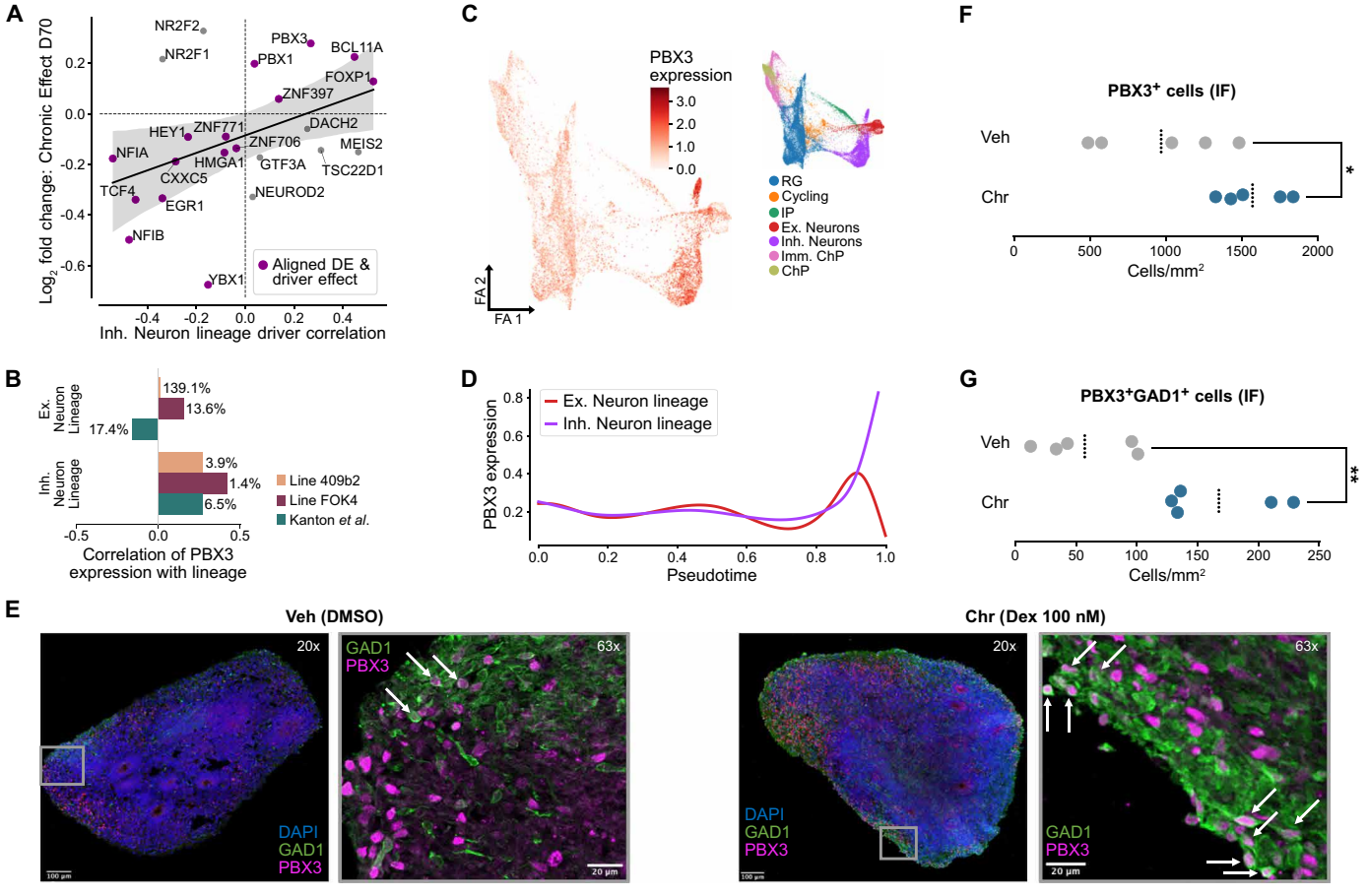

Fig. 6. PBX3 regulation through chronic GC exposure supports inhibitory neuron priming. (**A**) Magnitude of driver gene correlation with the inhibitory neuron lineage in the validation data (*43*) versus $\log_2$FC of GC day 70 DE effect measured in our two cell lines. Genes with aligned direction of $\log_2$FC and lineage correlation are marked in purple. (**B**) Correlation of *PBX3* expression with lineage probability across the excitatory and inhibitory neuronal lineages in all three datasets. The percentile of *PBX3* among all significant driver genes ranked by driver strength is shown on the side of every bar. (**C**) Expression of *PBX3* on a force-directed graph embedding of Line 409b2 data (left) with cell type reference (right). (**D**) Expression patterns of *PBX3* across pseudotime for each of the two neuronal lineage endpoints in Line 409b2. (**E**) Coexpression of GAD1$^+$ (green) cells with PBX3$^+$ (magenta) cells in 70-day-old ventralized organoids of Line 409b2 in Veh and Chr conditions. The ×63 magnification zoom-in images are shown to the right of the respective 20× whole-slice images. Examples of double-positive cells are marked by white arrows. (**F**) Cell counting quantification of PBX3$^+$ cells across entire organoid tissue slices ($n = 5$ per condition) and graphically represented as cells/mm^2. Means per condition are indicated as a dotted black line. Statistical significance was computed using an unpaired *t* test. (**G**) Cell counting quantification of PBX3$^+$GAD1$^+$ double-positive cells across entire organoid tissue slices ($n = 5$ per condition) and graphically represented as cells/mm^2. Means per condition are indicated as a dotted black line. Statistical significance was computed using an unpaired *t* test.

NEUROD2, *NFE2L2*, *NFIA*, *NFIB*, *NR2F1*, *NR2F2*, *NRG1*, *PBX3*, *SALL2*, *SOX2*, *TFAP2A*, and *YBX1* (table S8). Of these responsive TFs, the GC-up-regulated hox-gene *PBX3* was a positive inhibitory neuron lineage priming driver. At the same time, *NFIA*, *NFIB*, *EGR1*, and *YBX1* were down-regulated after GC exposure and negatively correlated with the inhibitory neuron lineage in the validation data. All five TFs could thus potentially contribute to the same priming effect. However, *PBX3* was the only TF that consistently was among the top 10% of driver genes for the inhibitory lineage in all three datasets (top 1.4 to 6.5%, depending on dataset) while not being among the top 10% of drivers for the excitatory neuron lineage in any of the datasets (Fig. 6B and fig. S4A). Therefore, we focused our further analysis on *PBX3* as an example of a GC-responsive TF, which could be involved in priming the inhibitory neuron lineage. We found *PBX3* to be expressed across all cell types, with the highest expression levels in inhibitory neurons (Fig. 6C and fig. S4B). *PBX3* has previously been linked to hindbrain-associated functions such as breathing, locomotion, and sensation (*47*).

The association of *PBX3* with the inhibitory lineage was supported by investigating the expression trends of *PBX3* along pseudotime and toward each of the two neuronal lineage endpoints, where it increased with advancing pseudotime, with the highest expression seen in inhibitory neurons (Fig. 6D and fig. S4B). Exploring data from the most recent atlas of the developing human brain (*48*), we found *PBX3* expression to be developmentally regulated and with overall higher expression in gamma-aminobutyric acid (GABA)-ergic compared to glutamatergic neurons and also higher in nontelencephalic compared to telencephalic brain regions (with highest expression in the cerebellum) (fig. S4C). This supports a consistent role of *PBX3* in the developing fetal brain and neural organoids.

In line with a priming effect of *PBX3* on inhibitory neurons, we observed an increased fraction of not only $PBX3^+$ at the transcriptional level in the Chr condition compared to the Veh condition across all cells in both cell lines (from 21 to 26% in Line 409b2 and from 22 to 38% in Line FOK4) but also $PBX3^+GAD1^+$ double-positive cells (from 1.7 to 3.9% in Line 409b2 and from 4.5 to 8.5% in Line FOK4). In both cell lines, the expression of *PBX3* and *GAD1* was significantly positively correlated in cells expressing both genes (Line 409b2: $r = 0.43$, $P = 4.1 \times 10^{-16}$; Line FOK4: $r = 0.36$, $P = 2.8 \times 10^{-15}$) (fig. S4D).

Using immunofluorescent labeling of the PBX3 protein, we imaged the ventrally guided organoids with GFP-tagged GAD1 at day 70 following chronic GC exposure, as previously described. We found protein-level expression patterns consistent with the scRNA-seq data, whereby PBX3 was identified preferentially (though not exclusively) in the more mature neurons that had already migrated to the outer ventricular zone (Fig. 6E). As with GAD1, we quantified $PBX3^+$ cells across entire organoid slices and found a 1.73-fold significantly increased abundance in chronically GC-exposed organoids compared to controls ($P = 0.022$; Fig. 6F and table S7). Given the apparent colocalization of the $GAD1^+$ and $PBX3^+$ cell populations (Fig. 6E), we also counted $PBX3^+GAD1^+$ double-positive cells and identified a 3.35-fold increase following GC exposure ($P = 0.0041$; Fig. 6G and table S7).

Having identified PBX3 as an example of a lineage-driving TF that responds robustly to GC treatment in our data, these results suggest a possible involvement of PBX3 in the priming of the inhibitory neuron lineage.

Multimodal analyses of gene regulatory networks associate PBX3 with the regulation of inhibitory neuron priming in organoids from Line 409b2

To understand the contribution of epigenetic regulation, we introduced another data modality with the same exposure paradigm. We collected scATAC-seq data for 90-day-old treated and control organoids of Line 409b2 (Veh-Veh and Chr-Veh condition). In Line 409b2, analyzed by itself, we still observed a significant positive correlation ($r = 0.077$, $P = 0.046$) between the DE effect in inhibitory neurons at day 70 (comparing Veh to Chr condition). This correlation increased at day 90, after 20 days of washout (comparing Veh-Veh to Chr-Veh condition) ($r = 0.15$, $P = 4.7 \times 10^{-3}$), supporting a lasting effect of the treatment on the cells committed toward this lineage (Fig. 7A).

Combining the scRNA-seq data with the additional scATAC-seq data enabled us to construct gene regulatory networks (GRNs) for treatment and vehicle organoids. To better understand the gene regulatory mechanisms underlying inhibitory neuron lineage priming at both vehicle and GC-exposed conditions, we integrated the single-cell genome accessibility data with the matching scRNA-seq data (Fig. 7B). We inferred multimodal GRNs using the expression of TFs and their target genes, accessibility of TF binding sites, and previous biological information such as conserved regions of the genome (table S9). Centering the GRN inferred in the vehicle organoids around *PBX3* allowed us to visualize the baseline regulatory interactions downstream of this TF. Notably, we found that in this TF-centered GRN, 35% of all genes were DE in at least one of the three GC treatment conditions (Veh versus Chr, Veh-Veh versus Chr-Veh, and Veh-Veh versus Veh-Acu) (Fig. 7C). This again highlights the role of *PBX3* in mediating the transcriptional response to GC exposure.

We computed the same *PBX3*-centered GRN for GC-exposed organoids and compared them to the baseline GRN. We found that 36% of direct downstream targets in the GC-exposed condition had been gained compared to the vehicle condition, and 30% of genes downstream of *PBX3* were among the top 500 drivers of the inhibitory neuron lineage (Fig. 7D). This finding agrees with our previous observation that large fractions of the GRN are responsive to GCs and relevant for the inhibitory neuron lineage.

Comparing the association of *PBX3* with the top 500 inhibitory drivers between the vehicle and GC-exposed *PBX3*-centered GRNs, we observed a pronounced relative increase of 32% (from 0.54 to 0.71) in the fraction of inhibitory neuron driver genes in its direct downstream targets (Fig. 7D). In particular, some genes with a large fold change in expression after exposure to GCs and a high correlation with the inhibitory neuron lineage were direct or second-order targets of *PBX3* in the GRN of organoids exposed to GC. Examples included *CELF4*, a gene associated with synaptic development (*49*), depression-like behavior in mice (*50*), and ASD (*51*). Another example was *SYNPR*, a common inhibitory neuron marker gene (Fig. 7A) (*52*, *53*). Overall, these results further support a role of *PBX3* in the priming of or the selection toward the inhibitory neuron lineage.

To further investigate the role of *PBX3* in priming the inhibitory neuron lineage, we used CellOracle (*54*) to carry out two in silico GRN perturbation experiments. In the first experiment, we perturbed a GRN based on the scRNA-seq and scATAC-seq data from 90-day-old control organoids of Line 409b2 (Veh-Veh condition; fig. S5A). Here, we simulated the effect of an increase in *PBX3* expression to 1.0 log-normalized counts by propagating the perturbation signal through the GRN. We computed a perturbation score by

Downloaded from https://www.science.org at Helmholtz Zentrum Mnchen - Zentralbibliothek on April 09, 2025

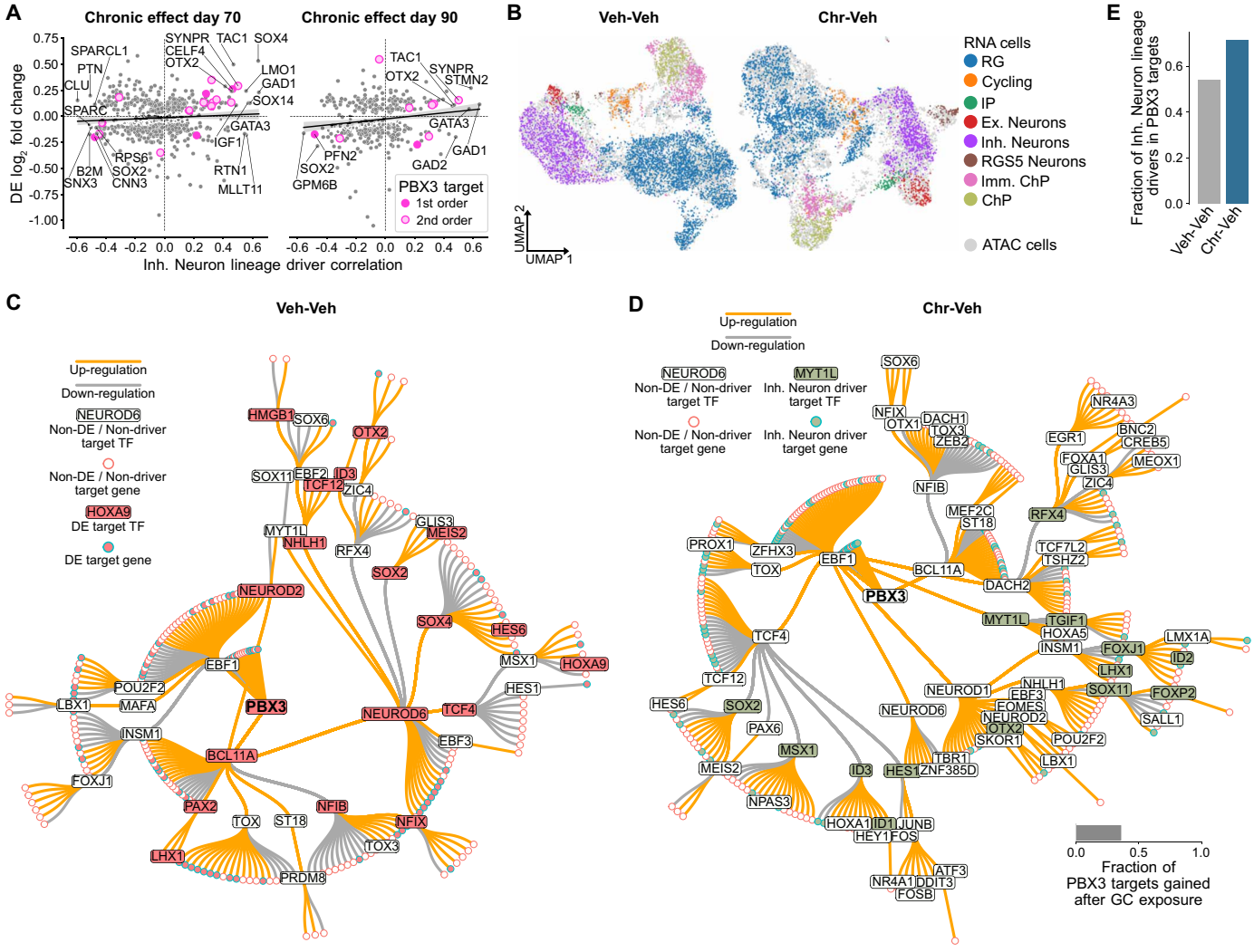

Fig. 7. Analyses of multimodal GRNs associate *PBX3* with the regulation of inhibitory neuron priming in organoids from Line 409b2. (**A**) Magnitude of driver gene correlation with the inhibitory neuron lineage versus log_2FC of Line 409b2. First- and second-order *PBX3* target genes in the inferred chronic GRN are labeled in pink. Left: Directly following treatment (70 days in culture). Right: After 20 days of washout (90 days in culture). Genes with an absolute lineage correlation greater than 0.45 are labeled by name. (**B**) UMAPs of integrated scRNA-seq and scATAC-seq data of Line 409b2 at 90 days in culture. ScRNA-seq data are colored by cell type, and scATAC-seq data are shown in gray. Left: Vehicle organoid data. Right: GC-exposed organoid data. (**C**) GRN centered around *PBX3* in vehicle organoids with DE genes (consensus DE genes from any of the three DE comparisons: D70 Chr, D90 Chr, D90 Acu) colored in red and TFs labeled by name. (**D**) GRN centered around *PBX3* in treated organoids with top 500 inhibitory neuron driver genes colored in green and TFs labeled by name. The bar chart shows the fraction of newly gained direct PBX3 downstream targets. (**E**) Fraction of inhibitory neuron drivers in direct TF downstream targets for control (Veh-Veh) and GC-exposed organoids (Chr-Veh) of Line 409b2 at 90 days in culture.

contrasting the shift in cell identity following perturbation with the natural differentiation vectors derived from the pseudotime computations. We observed marked positive perturbation scores for the inhibitory neuron lineage, suggesting that an increased *PBX3* expression would promote inhibitory neuron differentiation. The scores for the excitatory neuron lineage were also positive but much smaller than for the inhibitory lineage, while progenitor cells showed negative perturbation scores (fig. S5B). These results align well with our observed phenotype of increased neuronal differentiation, especially for the inhibitory neuron lineage, following chronic GC exposure, and support a central role of *PBX3* in priming the inhibitory neuron lineage.

We further validated our findings in a second in silico GRN perturbation experiment. Here, we simulated the effect of a full *PBX3* knockout (KO) in the independent scRNA-seq and scATAC-seq datasets from 90-day-old GC-exposed organoids of Line 409b2 (Chr-Veh condition). We found that this resulted in inverse perturbation scores with respect to the previous experiment. Specifically, we observed negative perturbation scores in the neuronal cells with a more pronounced effect in the inhibitory neurons and a positive perturbation score in the progenitor cells (fig. S5C). Together, these results suggest that a loss of *PBX3* expression in GC-exposed organoids would reverse the effect of increased differentiation and priming of the inhibitory neuron lineage. To confirm these results

Downloaded from https://www.science.org at Helmholtz Zentrum Mnchen - Zentralbibliothek on April 09, 2025

independently of our scATAC-seq data, we repeated the same two perturbation experiments using the CellOracle prebuilt human promoter base-GRN. We observed nearly identical perturbation scores compared to our initial results for both simulation experiments (fig. S5D).

DISCUSSION

Here, we investigated the effects of chronic exposure to GCs on cell type–specific gene regulation and lineage specification in neural organoids. Our experimental paradigm modeled common environmental challenges to the developing brain, specifically the prenatal administration of synthetic GCs. We observed highly cell type–specific gene expression changes directly following GC exposure that were sustained in various key molecular and cellular pathways even beyond a 20-day washout period. More than half of the lasting transcriptional changes after washout were shared with the transcriptional response to an acute GC exposure at day 90, supporting their relation to GR activation. In addition, transcripts regulated directly after chronic exposure converged on increased neuronal differentiation. We observed a positive correlation of the DE effect following GC exposure with expression changes driving the inhibitory neuron lineages, significantly more so than for excitatory neuron lineages. In line with promoting inhibitory lineage specification, in this brain model system, we showed that GC exposure led to a higher proportion of *GAD1*-positive cells, a canonical marker for inhibitory neurons, that lasted following the washout. This suggests that GCs shift neuronal developmental trajectories from excitatory to inhibitory neuronal patterns.

We identified *PBX3* as an example of an important TF for GC-induced promotion of the inhibitory neuron lineage, with both *PBX3* and its downstream targets being responsive to GCs and enriched for driver genes of the inhibitory neuron lineage. GC exposure led to an increased number of cells double-positive for *PBX3* and *GAD1*, supporting the role of this TF in GC-induced promotion of the inhibitory lineage. In silico perturbation experiments supported the role of *PBX3* in mediating the observed inhibitory neuron priming phenotype and suggested a potentially causal role of this TF. However, further experiments are required to confirm this and to elucidate a candidate mechanism of *PBX3* activation through GR-receptor (*NR3C1*) activation. Other TFs identified through this analysis to be regulated by GCs were previously identified as ASD risk genes and involved in altered inhibitory lineage specification (*29*). This highlights the convergence of environmental and genetic risk factors on neurodevelopment, not only on specific candidate genes but also on cellular trajectories.

Previous data from our group indicated that the expression of the GC receptor gene, *NR3C1*, increases in vitro until about day 40 when levels start to plateau until day 158 in organoids generated with a similar unguided protocol (*22*). Our 10-day treatment scheme (starting at day 60) and washout would thus fall within a window of continuously high *NR3C1* expression at the whole organoid level. Previous studies in a 2D cell culture context have described that chronic exposure to GC can alter neural cell proliferation and viability (*55*). Here, neural organoids may be especially vulnerable as they have been shown to contain cells in nonphysiological glycolytic or hypoxic states, likely caused by a lack of vasculature (*56*, *57*). Analyzing scRNA-seq data from organoids, especially in a chronic treatment context, thus requires particular care to account for metabolic profiles and altered cell states. Thus, we followed a previous study that suggested removing cells in nonphysiological states to facilitate the analysis and interpretation of neural organoid scRNA-seq data (*30*). This additional QC step allowed us to resolve the identity of an otherwise ambiguous cluster in both our datasets and improved the visualization of neuronal differentiation trajectories. It furthermore ensured that treatment and vehicle conditions had comparable cell viability scores (Fig. 2C).

scRNA-seq and scATAC-seq datasets were generated from experiments using an unguided organoid differentiation protocol, which enables the generation of a large variety of neural cell types in vitro (*58*). Regionalized organoid differentiation protocols, on the other hand, usually generate a more limited number of cell types with more regional or functional brain specificity. Notably, the exact neuronal lineages in organoids from unguided protocols can be challenging to predict a priori and do not always represent all brain regions. Therefore, a careful evaluation of the identity of obtained cell types is required so that results can be interpreted in the proper context. Mapping our datasets to the Human Neural Organoid Cell Atlas (*36*) enabled precise and efficient identification of cell types. It revealed an overlapping cell identity for nontelencephalic excitatory and inhibitory neurons, nontelencephalic NPCs, and a more limited range of glial and choroid plexus cells as expected for the brain maturity level replicated by organoids at the chosen stage.

The abundance of nontelencephalic neurons was likely an enabling factor for identifying *PBX3* as a strong GC-induced inhibitory lineage driver. In a focused analysis of *PBX3* expression in the developing fetal brain (*48*), we observed that this TF is developmentally regulated, with higher expression in GABAergic neurons and the highest levels observed in the cerebellum (fig. S4C). The reported effects of GCs may thus be restricted to nontelencephalic brain regions and not necessarily extrapolate to telencephalic neurons. We did, however, also find *PBX3* to be a strong and specific driver of the telencephalic inhibitory neuron lineage in the dataset by Kanton *et al.* (*43*). Likely due to its graded expression, with highest levels in the hindbrain, including the brainstem and cerebellum, and lowest levels in the telencephalon, only very little data on the role of *PBX3* in human brain development have been reported since most previous studies in vivo and in vitro have focused on the telencephalon. However, the hindbrain has been of increasing interest in NDDs, including ASD, with several studies pointing to a potentially important role of hindbrain structures, such as the cerebellum and the brainstem, in these disorders (*59*–*61*).

Our results also support the key role of the excitatory/inhibitory balance in the pathogenesis of mental and neurodevelopmental disorders and the fact that genetic and environmental risk factors converge on this same phenotype. While previous studies have identified converging effects of genetic and environmental risk factors for ASD and NDD, for example, with respect to endocrine disruptors altering the expression of NDD and autism-associated genes and with respect to protective effects of estrogens in this context (*62*, *63*), our article highlights an additional convergence at the level of lineage determination and cell fate specification within the neuronal lineage. Previous studies in different human cellular and genetic models of ASD (*24*–*28*) and data from CRISPR-based perturbation assays in neural organoids confirm the critical role of inhibitory neurons in the pathomechanisms of these disorders. Perturbation assays targeting ASD and other NDD candidate genes have shown that they directly affect lineage specification toward inhibitory

Downloaded from https://www.science.org at Helmholtz Zentrum Mnchen - Zentralbibliothek on April 09, 2025

neuronal cells (*29*) and migration of inhibitory neurons (*4*). Given our findings on the effects of GC exposure on *PBX3* and inhibitory neuron lineages, it would now also be important to examine the effects of other known environmental risk factors on this phenotype. In addition, previous data from our group indicates the relevance of the timing of the exposure. GC exposure in dorsal pallial ventricular structures at an earlier developmental time point (days 43 to 50) led to an increase in a specific progenitor type enriched in gyrencephalic species contributing to increased neurogenesis (*23*). Our results regarding an exposure later in the timeline of neurodevelopment reaffirm the effect of GCs on increasing neurogenesis during critical developmental windows, with a concomitant shift in lineage specification toward inhibitory neurons. This highlights GCs as important drivers of neurogenesis for inhibitory and excitatory neuronal lineages with a more pronounced effect on the former at later time points. Additional experiments examining more extended time windows will be necessary to understand all possible timing and combinatorial effects.

Despite relevant advances in knowledge, our study has some limitations worthy of note. One is the use of only female-derived cell lines for organoid generation for our primary experiments, which prevents us from uncovering possible sex-specific differences in lineage priming after GC exposure. Previous studies that included male and female lines have not revealed sex-specific differences in the molecular or cellular response to GC (*22*, *23*), but were likely underpowered in this regard. To further dissect potential sex differences, investigation of a larger number of cell lines will be necessary (*64*), as well as potential coadministration of sex steroids, as these differ between sexes early in gestation (*65*). Placental secretion of the first wave of sex hormones begins with testosterone as early as gestational week 8, and peaks around gestational week 14, therefore overlapping with the peak of neurogenesis (*66*). In line with this, Kelava *et al.* (*67*) have shown effects of testosterone but not the complement of sex chromosomes alone on neurogenesis in cerebral organoids.

Using unguided organoid differentiation protocols enabled us to investigate the effect of GC exposure on a broad range of stem, progenitor, and neuron subtypes. At the same time, this inherently meant that the exact brain regions recapitulated by our organoids were not guided by any additional morphogens in the culture medium. Organoids from both cell lines recapitulated almost exclusively different neuronal subtypes from nontelencephalic regions of the brain, specifying our analyses to these brain regions. While there is growing evidence for the importance of such nontelencephalic regions like the hindbrain in the development and manifestation of NDDs (see paragraph above), telencephalic structures also play a central role. To fully capture the effects of GC exposure on lineage priming in the developing human brain, further investigations using an organoid system recapitulating both excitatory and inhibitory telencephalic neuron lineages would be required. Therefore, common cortical organoids alone would not be sufficient for this task, and advanced organoid technologies such as assembloids would represent an interesting future avenue to answer these questions (*68*).

Another limitation originates from our deliberately conservative DE analysis approach. We chose to not focus on any DE genes without agreeing significance and direction of effect between the two hiPSC lines, focusing our analysis on transcriptional changes that occur independent of genetic background or differences in *NR3C1* expression levels for increased robustness. Adding organoids derived from additional hiPSC lines to the analysis will likely increase the power to detect additional and shared GC-regulated transcripts that were not uncovered here.

Overall, this study highlights the complex interplay between GC exposure, TF regulation, lineage specification, and neurodevelopment. It provides a molecular and cellular link between genetic and environmental risk factors for NDDs, including ASD. These results also open up new avenues of investigation. Applying chronic GC treatment at different developmental time points could elucidate whether selective lineage priming is associated with varying timing of differentiation across neuronal subtypes. Probing the downstream targets and interaction partners of these TFs would provide insights into the molecular pathways involved in inhibitory lineage priming. In vitro model systems could be used to investigate potential rescue mechanisms following lineage divergence in the context of environmental exposures. Uncovering these mechanisms can deepen our understanding of normal brain development and shed light on the molecular cascades contributing to NDDs.

MATERIALS AND METHODS

iPSC culture, neural organoid generation, and GC treatment

iPSCs

Two primary hiPSC lines were used in this study. The first cell line was reprogrammed from skin fibroblasts using well-established protocols and made commercially available by the Riken institute (HPS0076:409b2, RIKEN BRC cell bank, female) (*69*, *70*). Henceforth, this line is referred to as "Line 409b2" in this article. The second cell line was reprogrammed in-house using a plasmid-based protocol for integration-free hiPSCs from peripheral blood mononuclear cells from a female donor through the BeCOME study (*71*) and is referred to as "Line FOK4" in this article. Validation of hiPSC status for this line was performed in-house using standard immunofluorescence staining with pluripotency markers and shown in OCT4, NANOG, and TRA-160. Briefly, staining with the following is shown in fig. S6B: Anti-Human Oct-4 Antibody (Millipore, ABD116), rabbit polyclonal, Anti-NANOG Antibody, clone 7F7.1 (Millipore, MABD24), mouse monoclonal, Anti-TRA-1-60 Antibody, clone TRA-1-60 (Millipore, MAB4360), mouse monoclonal. Comparable validation for line 409b2 was performed by the Riken institute and shown in (*69*, *70*). Material transfer agreement (MTA) for the use of the 409b2 line was obtained from the Riken institute according to their standard policies and approval by the Ludwig Maximilian University of Munich ethics committee. The in-house reprogrammed FOK4 line can be provided by the corresponding authors pending scientific review and a completed MTA. Requests should be submitted to E.B.B. hiPSCs were cultured in Matrigel-coated [1:100 diluted in Dulbecco's modified Eagle's medium (DMEM)/Nutrient Mixture F12 (Gibco, 31330-038), Corning Incorporated, 354277] Costar six-well cell culture plates (Corning Incorporated, 3516) in mTESR1 Basal Medium (STEMCELL Technologies, 85851) supplemented with 1× mTESR1 Supplement (STEMCELL Technologies, 85852) at 37°C with 5% CO_2. Passaging was performed with Gentle Cell Dissociation Reagent (STEMCELL Technologies, 07174). RevitaCell Supplement (1:100 diluted, Gibco, A2644501) was added for 24 hours after passaging to promote cell survival. To assess the genomic stability of hiPSCs before organoid generation, digital karyotyping was performed using the Infinium

Downloaded from https://www.science.org at Helmholtz Zentrum Mnchen - Zentralbibliothek on April 09, 2025

Global Screening Array-24 v3.0 BeadChip (Illumina). A pairwise copy number variant analysis was performed for both hiPSC lines, comparing the hiPSC genotype at the passage before differentiation to the original donor from a blood or fibroblast sample. No significant deviations were detected for either 409b2 or FOK4 (fig. S6A).

Neural organoids

Human neural organoids were created as described by Lancaster and Knoblich (*58*) with some modifications. Briefly, hiPSCs were dissociated in StemPro Accutase Cell Dissociation Reagent (Life Technologies, A1110501). Single cells (n = 9000) were dispensed into each well of an ultra-low attachment 96-well plate with round bottom wells (Corning Incorporated, 7007) in human embryonic stem cell (hESC) medium [DMEM/F12-GlutaMAX (Gibco, 31331-028) with 20% Knockout Serum Replacement (Gibco, 10828-028), 3% FBS (fetal bovine serum; Gibco, 16141-061), 1% nonessential amino acids (Gibco, 11140-035), 0.1 mM 2-mercaptoethanol (Gibco, 31350-010)] supplemented with human recombinant FGF (fibroblast growth factor; 4 ng/ml; PeproTech, 100-18B) and 50 μM Rock inhibitor Y27632 (Millipore, SCM075) for 4 days and in hESC medium without basic fibroblast growth factor (bFGF) and Rock inhibitor for an additional 2 days to form embryoid bodies (EBs). On day 6, the medium was changed to neural induction medium [NIM; DMEM/F12 GlutaMAX supplemented with 1:100 N2 supplement (Gibco, 15502-048), 1% nonessential amino acids, and heparin (1 μg/ml; Sigma-Aldrich, H3149)] and cultured for an additional 6 days. On day 12, the EBs were embedded in Matrigel (Corning Incorporated, 354234) drops and transferred to 10-cm cell culture plates (TPP, 93100) in neural differentiation medium without vitamin A [NDM-A; DMEM/F12 GlutaMAX and Neurobasal (Gibco, 21103-049) in a 1:1 ratio, additionally supplemented with 1:100 N2 supplement 1:100 B27 without vitamin A (Gibco, 12587-010), 0.5% nonessential amino acids, insulin (2.5 μg/ml; Gibco, 19278), 1:100 antibiotic-antimycotic (Gibco, 15240-062), and 50 μM 2-mercaptoethanol] for 4 days. On day 16, organoids were transferred onto an orbital shaker in NDM+A medium [same composition as NDM-A with the addition of B27 with vitamin A (Gibco, 17504-044) in the place of B27 without vitamin A] and were grown in these conditions at 37°C with 5% CO_2. NDM+A medium was changed twice per week until the organoids were collected for cryopreservation or single-cell dissociation or fixation in paraformaldehyde (PFA).

For validation of inhibitory-excitatory neural lineage effects of GC, guided ventral organoids were generated as previously described by Bagley *et al.* (*46*). Briefly, EBs were formed starting from iPSCs dissociated into single cells using Accutase (Sigma-Aldrich, A6964) (n = 9000). Five days later, during the neuronal induction, to induce brain regionalization, EBs were treated individually with smoothened agonist (1:10,000) (Millipore, 566660) + IWP-2 (1:2000) (Sigma-Aldrich, I0536) for ventral identity and with cyclopamine A (1:500) (Calbiochem, 239803) for dorsal identity. All other culture parameters were identical to the ones described above for unguided organoids.

Generation and validation of a neuron-specific fluorescent reporter iPSC cell line

Line 409b2 hiPSCs were used to generate an $eGFP^+/GAD1^+$ heterozygous iPSC cell line. Guide RNA (gRNA) [crRNA and tracrRNA, Integrated DNA Technologies (IDT)] for editing with the recombinant S.p. HiFi Cas9 Nuclease V3 protein (IDT) was selected to cut efficiently at a short distance from the ATG start codon of the *GAD1* gene by using the Benchling web tool (https://benchling.com). A 1611-nucleotide (nt) donor ssODNs (IDT) for homology-directed recombination was designed to have homology arms of 222 to 300 nt on either side of the insert DNA and a 717-nt sequence encoding for enhanced GFP (eGFP) followed by the 3′ untranslated region and the polyA signal. Lipofection (reverse transfection) was performed using the alt-CRISPR manufacturer's protocol (IDT) with a final concentration of 10 nM of the gRNA, ssODN donor, and Cas9. In brief, 0.75 μl of RNAiMAX (Invitrogen, 13778075) and the RNP mix (gRNA, ssODN, and Cas9 protein) were separately diluted in 25 μl of Opti-MEM (Gibco, 1985-062) each and incubated at room temperature for 5 min. Both dilutions were mixed to yield 50 μl of Opti-MEM. The lipofection mix was incubated for 20 to 30 min at room temperature. During incubation, cells were dissociated with Accutase (Life Technologies) for 6 min and counted. The lipofection mix, 100 μl containing 50,000 dissociated cells in mTeSR1 supplemented with RevitaCell (1:100, Gibco) and the 2 μM M3814 NHEJ inhibitor (*72*), was thoroughly mixed and placed in 1 well of a 96-well plate covered with Matrigel matrix (Corning, 35248). The medium was exchanged to regular mTeSR1 medium (STEMCELL Technologies) containing the NHEJ inhibitor after 24 hours. Single cell–derived clonal cell lines were analyzed and genotyped by polymerase chain reaction (PCR) using genomic DNA isolated with QuickExtract DNA Extraction Solution (Lucigen) and primers binding within and downstream the modified region (Primer 1) or in the homology arms (Primer 2).

gRNA 5′_GGTCGAAGACGCCATCAGCT_3′

ssODN 5′_*TGCGCACCCCTACCAGGCAGGCTCGCTGCCTT-TCCTCCCTCTTGTCTCTCCAGAGCCGGATCTTCAAGGGGAGCC-TCCGTGCCCCCGGCTGCTCAGTCCCTCCGGTGTGCAGGACCCCG-GAAGTCCTCCCCGCACAGCTCTCGCTTCTCTTTGCAGCCT-GTTTCTGCGCCGGACCAGTCGAGGACTCTGGACAGTAGAG-GCCCCGGGACGACCGAGCTG*<u>*ATG*</u>GTGAGCAAGGGCGAG-GAGCTGTTCACCGGGGTGGTGCCCATCCTGGTCGAGCTG-GACGGCGACGTAAACGGCCACAAGTTCAGCGTGTCCGGC-GAGGGCGAGGGCGATGCCACCTACGGCAAGCTGACCCT-GAAGTTCATCTGCACCACCGGCAAGCTGCCCGTGCCCTG-GCCCACCCTCGTGACCACCCTGACCTACGGCGTGCAGT-GCTTCAGCCGCTACCCCGACCACATGAAGCAGCAC-GACTTCTTCAAGTCCGCCATGCCCGAAGGCTACGTCCAG-GAGCGCACCATCTTCTTCAAGGACGACGGCAACTA-CAAGACCCGCGCCGAGGTGAAGTTCGAGGGCGACACCCTG-GTGAACCGCATCGAGCTGAAGGGCATCGACTTCAAGGAG-GACGGCAACATCCTGGGGCACAAGCTGGAGTACAACTACAA-CAGCCACAACGTCTATATCATGGCCGACAAGCAGAAGAACG-GCATCAAGGTGAACTTCAAGATCCGCCACAACATCGAGGAC-GGCAGCGTGCAGCTCGCCGACCACTACCAGCAGAA-CACCCCCATCGGCGACGGCCCCGTGCTGCTGCCCGACAAC-CACTACCTGAGCACCCAGTCCGCCCTGAGCAAAGACCCCAAC-GAGAAGCGCGATCACATGGTCCTGCTGGAGTTCGTGACCGC-CGCCGGGATCACTCTCGGCATGGACGAGCTGTACAAG*<u>*TAA*</u>*C-TAGAGCTCGCTGATCAGCCTCGACTGTGCCTTCTAGTTGC-CAGCCATCTGTTGTTTGCCCCTCCCCCGTGCCTTCCTT-GACCCTGGAAGGTGCCACTCCCACTGTCCTTTCCTAATA-AAATGAGGAAATTGCATCGCATTGTCTGAGTAGGTGTCATTC-TATTCTGGGGGGTGGGGTGGGGCAGGACAGCAAGGGGGAG-GATTGGGAAGACAATAGCAGGCATGCTGGGGATGCG-GTGGGCTCTATGGCTTCTGAGGCGGAAAGAAC-CAGCTGGGGCTCTAGGGGGTATCCCCGCGTCTTC-GACCCCATCTTCGTCCGCAACCTCCTCGAACGCGGGAGCG-*

Downloaded from https://www.science.org at Helmholtz Zentrum Mnchen - Zentralbibliothek on April 09, 2025

GACCCCAATACCACTAACCTGCGCCCCACAAGTAGGTCCC-GCCCCAATTTTCTATCAAATGAACTGCAGGGAA-GATGGGGGCGCTGGGACGTCGGGAGGCTGAGCTGGCG-GAAAGGGAAGGGGGAGCGCGGAGATAATGGAG-GCTGGGAAATAAATGGGGCTCTGACCCCGTCCCTGCCAGAG-GTCATTCGGCTGTCAGGGACGCTAGGTGACTCCCAGGGCACC-GGAAAGCGAGGACCACGCAAGGTCCGA_3′

Left and right homology arms are indicated in italics. eGFP start and stop codons are underlined.

GFP protein translation:

MVSKGEELFTGVVPILVELDGDVNGHKFSVSGEGEGDA-TYGKLTLKFICTTGKLPVPWPTLVTTLTYGVQCFSRYP-DHMKQHDFFKSAMPEGYVQERTIFFKDDGNYKTRAEVK-FEGDTLVNRIELKGIDFKEDGNILGHKLEYNYNSHNVY-IMADKQKNGIKVNFKIRHNIEDGSVQLADHYQQNT-PIGDGPVLLPDNHYLSTQSALSKDPNEKRDHMVLLEFVTA-AGITLGMDELYK*

Primer 1	For 5′_CACTCCCACTGTCCTTTCCTAA_3′
	Rev 5′_TCCTAGCTCTTCATTCCGCC_3′
Primer 2	For 5′_GCTTCTCTTTGCAGCCTGTTTC_3′
	Rev 5′_GGGCGCAGGTTAGTGGTATT_3′

Dexamethasone treatment

Organoids were treated with GCs by dissolving Dexamethasone (Dex) in DMSO (dimethyl sulfoxide) and subsequently in the NDM+A culture medium. To achieve the final concentration of 100 nM, Dex was first diluted in DMSO in a concentration of 100 μM and subsequently diluted in NDM+A culture medium to a final concentration of 100 nM. Vehicle control (Veh) organoids received equal amounts of DMSO. Chronic exposures (days 60 to 70 in culture) were performed by replacing supplemented medium every 2 days. Some organoids were collected at day 70 following 10 days of exposure. Other organoids from the same batch were subsequently cultured in normal unsupplemented medium for a 20-day washout period followed by an acute exposure (day 90 in culture) with 100 nM Dex or DMSO for 12 hours. The timing for the treatment starting at day 60 was chosen to reflect a robust expression of the GR (*NR3C1*) and overlapping gene expression profiles with fetal brain tissue (*22*). The timing of the exposure and the washout was chosen based on previous experiments in a human hippocampal progenitor cell line that revealed lasting and functional changes in DNA methylation in relevant gene regulatory elements after 10-day exposure to Dex during neuronal differentiation and a subsequent 20-day washout (*73*).

Immunofluorescence

Organoids were fixed using 4% PFA for 45 min at 4°C, cryopreserved with 30% sucrose, fixed in optimal cutting temperature (OCT) compound (Thermo Fisher Scientific), and stored at −20°C before cutting and preparation of 16-μm cryosections on SuperFrost slides. Between two and three blocks of three to four organoids each were fixed per condition, leading to $n = 6$ to 12 organoids for staining and subsequent counting. For immunofluorescence, sections were postfixed using 4% PFA for 10 min and permeabilized with 0.3% Triton for 5 min. Sections were subsequently blocked with 0.1% Tween, 10% normal goat serum, and 3% bovine serum albumin (BSA). For staining with GFP and PBX3, the slides were put through antigen retrieval before fixing with PFA. More specifically, the slides were incubated in citric buffer (0.01 M, pH 6.0) for 1 min at 720 W and 10 min at 120 W, left to cool down at room temperature for 20 min, and washed once with phosphate-buffered saline (PBS). Alexa-anti-chicken-488 and Alexa-anti-rabbit-647 were used as secondary antibodies. All secondary antibodies are diluted to 1 μg/ml or 1:1000 in blocking solution.

Antibodies

Antigen	Dilution	Vendor	Catalog no.
DAPI	1:1000	Sigma-Aldrich	D9542
GFP	1:1000	Aves Lab	1020
PBX3	1:500	Abcam	ab52903
NeuN	1:500	Millipore	MAB377
OCT4	1:500	Millipore	ABD116
NANOG	1:250	Millipore	MABD24
TRA-160	1:250	Millipore	MAB4360

Cell imaging and counting

For immunofluorescence, stained slides were imaged using the 20× and 63× lens in confocal mode on the MICA Microhub microscope (Leica) and the Leica Application Suite X software (version 1.4.4.26810) or using the 20× lens on the AxioScan.Z1 Slide Scanner (Zeiss). To identify cells positively stained only for PBX3, NeuN, and GFP-GAD1 as well as cells double-positive for PBX3 and GFP-GAD1 or NeuN and GFP-GAD1, cells were manually counted by two independent experimenters in two separate staining experiments using the Cell Counter Tool in ImageJ software. A minimum of $n = 6$ whole organoids were used per condition. Specifically, between two and three blocks of OCT compound of three to four organoids each were fixed per condition, leading to $n = 6$ to 12 independent organoids used for staining, microscopy imaging, and subsequent counting. Counts are reported as cells/mm^2 normalized by tissue surface area. AxioScan.Z1 Slide Scanner images are quantified as total counts per entire organoid slice ($n = 5$ per group), while MICA Microhub images are quantified as one representative selected tile per mosaic organoid slide ($n = 10$ tiles per group). Statistical analyses are reported as two-sided unpaired *t* tests.

scRNA-seq library preparation and sequencing

Single cells were dissociated using StemPro Accutase Cell Dissociation Reagent (Life Technologies), filtered through 30- and 20-μm filters (Miltenyi Biotec), and cleaned of debris using a Percoll (Sigma-Aldrich, P1644) gradient. Single cells were resuspended in ice-cold PBS supplemented with 0.04% BSA and prepared for single-cell separation. Experiments were performed in a paired case-control design, with two or four conditions at day 70 and day 90, respectively, run in parallel. Single cells were run through the Chromium controller to form gel emulsion beads containing barcoded single cells and prepared into single-cell libraries using the Chromium Single Cell 3′ Reagent Kits v2 according to the manufacturer's recommendations without any modifications (10x Genomics). To reach an optimal target cell number, 10,000 cells per sample were loaded onto a channel of the 10x chip. All libraries were assessed using a High Sensitivity DNA Analysis Kit for the 2100 Bioanalyzer (Agilent) and KAPA Library Quantification kit for Illumina (KAPA Biosystems). Sequencing of the 10x Genomics single-cell RNA-seq libraries was performed on an Illumina NovaSeq 6000 (Illumina, San Diego, CA) at the sequencing core facility of the Max Planck Institute for Molecular Genetics (Berlin, Germany).

scATAC-seq library preparation and sequencing

Single cells were dissociated from whole organoids according to the scRNA protocol above. Subsequent nuclei preparation and scATAC-seq library generation were performed using the Chromium Single Cell ATAC Library & Gel Bead Kit (16 rxns PN-1000110) according to the manufacturer's recommendations without any modifications (10x Genomics). Sequencing of the 10x Genomics scATAC-seq

Downloaded from https://www.science.org at Helmholtz Zentrum Mnchen - Zentralbibliothek on April 09, 2025

libraries was performed on Illumina NovaSeq 6000 (Illumina, San Diego, CA) by the sequencing core facility at the Max Planck Institute for Molecular Genetics (Berlin, Germany).

Computational methods and analyses

scRNA-seq quality control

Count matrices were produced from fastq files using 10x Genomics Cell Ranger (*74*) v3.0.2 with the transcriptome hg38_ensrel94 (*75*). Count matrices of 90-day-old acutely treated and control organoids of Line 409b2 and Line FOK4 (Veh-Veh and Veh-Acu conditions) have previously been used by Cruceanu *et al.* (*22*) and are available from the Gene Expression Omnibus repository (accession: GSE189534). All data have been reprocessed and reanalyzed here.

All downstream analyses were carried out using the scverse (*76*) packages scanpy (*77*) v1.9.3 and anndata (*78*) v0.9.1 with Python v3.10.12 unless indicated otherwise. For QC, cells with less than 1200 total unique molecular identifier (UMI) counts, cells with more than 150,000 total UMI counts, cells with less than 700 genes expressed, and cells with 25% or more mitochondrial UMI counts were removed from the dataset. Next, any genes expressed in less than 20 cells were removed.

For a second QC step, an initial clustering of the full dataset was computed using louvain clustering (louvain Python package v0.8.0, https://github.com/vtraag/louvain-igraph) (*79*) with appropriate preprocessing and a resolution of 0.5. On the basis of this clustering, two samples, which mainly clustered separately from all other samples, were removed (409b2-D70-Chr-V1, 409b2-D70-Veh-V2). In addition, three further samples with low numbers of expressed genes or a sequencing saturation below 35%, as reported by 10x Genomics Cell Ranger, were removed (409b2-D70-Veh-C1, FOK4-D90-Veh-Veh-C1, FOK4-D90-Veh-Veh-C2).

For a final QC step, the data were reclustered following the same procedure as before, and marker genes were computed using the gene ranking function of scanpy with default parameters. On the basis of the marker gene signature, any clusters containing mostly mesenchymal cells, epithelial cells, myocytes, neuroectoderm, neural stem cells, macrophages, or fibroblasts were removed from the dataset.

scRNA-seq data preprocessing and cluster annotation

All steps described in this section were applied separately to the data derived from Line 409b2 and Line FOK4. Normalization size factors were computed using the scran (*80*) R package v1.22.1 (R v4.1.2) with the appropriate preprocessing to obtain an initial coarse clustering of the data as required for this approach. The raw counts of each cell were then normalized by the respective size factor and $\log(1 + x)$ transformed. Four thousand highly variable genes (HVGs) were computed using the log-normalized counts using the "cell_ranger" flavor (*74*). Principal components (*81*), a nearest neighbor graph (*82*), a force-directed graph drawing (https://github.com/bhargavchippada/forceatlas2) (*83*), louvain clustering (https://github.com/vtraag/louvain-igraph) (*79*), and partition-based graph abstraction (PAGA) (*84*) were computed using default parameters. The layout obtained from plotting the PAGA results with a threshold of 0.05 was used as initialization to compute Uniform Manifold Approximation and Projection (UMAP) (*82*) with default parameters.

Marker genes were computed by ranking genes for each cluster, with further subclustering or merging of clusters performed where appropriate. Cell type identities were assigned to clusters by comparing top-ranking genes per cluster with known marker genes from developmental neurobiology. A total of eight cell types and one cluster of unknown identity were identified using this procedure.

Removing nonviable cells from scRNA-seq datasets

All steps described in this section were applied separately to the data derived from Line 409b2 and Line FOK4. To identify cells in nonviable metabolic states, the following Gene Ontology (*85*, *86*) Biological Process gene sets were scored using the respective scanpy function with default parameters in every cell [as previously suggested (*30*)]. Negative markers of cell viability: "glycolytic process" (GO:0006096), "response to endoplasmic reticulum stress" (GO:0034976). Positive markers of cell viability: "gliogenesis" (GO:0042043), "neurogenesis" (GO:0022008), and previously reported marker genes of the choroid plexus (*87*). Each score was scaled to the range (0,1). A joint cell viability score was computed by adding all scaled positive viability scores, subtracting all scaled negative viability scores, and scaling the final score to the range (0,1). Cells with a final viability score of less than or equal to 0.4 were identified as nonviable cells and removed from the dataset. To further characterize the remaining cells of the Unknown cluster, marker genes of this cluster with respect to all other clusters were computed after the score-based nonviable cell removal. This was done using a *t* test through the rank_genes_groups scanpy function. Following analysis of the marker genes, the Unknown cluster was removed entirely from the dataset.

Following the removal of nonviable cells, HVGs, principal components, the neighbor graph, force-directed graph drawing, PAGA (threshold 0.001 for computing the layout), and UMAP were recomputed following the same procedure described in the section above.

Mapping scRNA-seq data to the human neural organoid cell atlas

Query to reference mapping using scPoli (*88*) from the scArches (*89*) package v0.5.9 was used to project the scRNA-seq data acquired in this study to the Human Neural Organoid Cell Atlas (HNOCA) (*36*). HNOCA data and the scPoli integration model weights used in the original study were obtained from https://github.com/theislab/neural_organoid_atlas. The feature (gene) space of the datasets from this study was adapted to the feature space used in the HNOCA scPoli model, filling any missing genes with zero expression. The query model was trained for five pretraining epochs and one training epoch with unlabeled prototype training enabled. Annealing of the model hyperparameter α was set to 10 epochs, and the model hyperparameter η was set to 5. Feeding this study's data and the HNOCA data through the trained model produced a mapped latent representation, which was used as input for the neighbor graph and UMAP computation. Cell type annotations from the "annot_level_2" HNOCA annotation column [the final annotation shown in figure 1 of the HNOCA paper (*36*)] were used to contextualize the data generated in this study.

scRNA-seq differential expression analysis

The R tool MAST (*90*) v1.20.0 (R v4.1.2) was used to compute DE genes per cell type between treatment conditions on log-normalized expression data. This analysis was carried out separately for the two source cell lines. Samples that contained less than 10 cells of a given cell type were removed to compute differential expression (DE) for this cell type. Additionally, genes expressed in less than 5% of cells of a given cell type were also removed to compute DE for this cell type. For each cell type and source cell line, a hurdle model was fit according to the following formula:

~ ngeneson + treatment_acute + treatment_chronic + treatment_chronic:treatment_acute

Downloaded from https://www.science.org at Helmholtz Zentrum Mnchen - Zentralbibliothek on April 09, 2025

where *ngeneson* corresponds to the number of expressed genes in the sample, *treatment_chronic* corresponds to the 10-day treatment applied between day 60 and day 70 (Veh or Chr), and *treatment_acute* corresponds to the 12-hour treatment applied at day 90 (Veh, Acu, or None for samples collected at 70 days in culture). A likelihood ratio test was applied to test for DE at day 70 (chronic effect) and day 90 (chronic and acute effect).

Only genes with an FDR-corrected *P* value of less than 0.1 in both source cell lines and agreeing direction of DE fold change were deemed DE for a given cell type to reduce the number of false-positive DE results. DE genes were visualized using the UpSetPlot (*91*) v0.8.0 Python package (https://github.com/jnothman/UpSetPlot).

Functional enrichment analysis of DE genes and TF target gene enrichment

Consensus DE genes computed as described in the previous section were used as input to the enrichment analysis using the Python implementation of Enrichr (*92*, *93*) via the GSEApy (*94*) package v1.0.5 with default parameters. For the annotation of biological function, the "GO_Biological_Process_2021" gene set was used as provided by Enrichr. For the TF target enrichments, the "ENCODE_and_ChEA_Consensus_TFs_from_ChIP-X" gene set was used as provided by Enrichr. For greater coverage of TFs, a second database was used for this enrichment: CollectTRI (*95*), obtained via the Python implementation of decoupler (*96*) v1.4.0. Any hits with an FDR of less than 0.1 were considered significantly enriched.

Gene Ontology enrichment results were summarized and visualized using GO-Figure (*97*) v1.0.1 (go.obo version: releases/2021-05-01; go.obo version used to create GO relations: releases/2023-04-01; similarity_cutoff: 0.2).

Processing of public neural organoid scRNA-seq data

Count data, associated metadata, and gene names were downloaded from ArrayExpress (accession: E-MTAB-7552) as stated in the data availability section of the Kanton *et al.* publication (*43*). The dataset was subset to cells belonging to the study's 70-day-old organoid cell line comparison section. Any cells from cell line 409b2 or cells without a cell type label were removed from the dataset. Genes expressed in less than 10 remaining cells were also removed from the dataset. Raw counts were normalized per cell to the median total counts per cell in the dataset and $\log(1 + x)$–transformed. HVGs and principal components were computed as with the original datasets. An integrated neighbor graph was computed using the BBKNN algorithm (*98*) (bbknn Python package v1.5.1) using cell line as a batch key and neighbors_within_batch = 5 with otherwise default parameters of the scanpy external implementation. From this integrated neighborhood graph, UMAP and force-directed graph drawing were computed with default parameters. The "Cortical neurons" cluster and the "LGE interneurons" cluster were identified as the excitatory and inhibitory neuron cell types in this dataset, respectively.

Trajectory inference and driver gene computation

For Line 409b2 and Line FOK4 data, the RGS5 Neurons cluster was removed from the dataset for this analysis, followed by recomputation of HVGs, principal components, the neighbor graph, force-directed graph drawing, PAGA (threshold 0.001 for computing the layout), and UMAP following the same procedure as described in the sections above. All the steps described in this section were applied separately to the data derived from Line 409b2, Line FOK4, and the external validation data.

The scanpy external implementation of Palantir (*99*) was used to compute a pseudotime following the manual selection of an "early cell" within a progenitor cluster for each dataset (RG for Line 409b2 and FOK4, cortical NPCs for the validation data). First, Palantir diffusion maps were computed with five diffusion components and otherwise default parameters. Second, a *t*-distributed stochastic neighborhood embedding (tSNE) (*100*) representation was computed on the first two components of the Palantir multiscale data matrix with a perplexity of 150 and otherwise default parameters. The resulting embedding was used to compute the Palantir pseudotime, sampling 500 waypoints and otherwise default parameters.

CellRank (*44*, *101*) was used to compute lineage probabilities based on the Palantir pseudotime. CellRank was installed from the GitHub main branch (https://github.com/theislab/cellrank) at commit c3ced63 (earliest stable version including this commit: v2.0.1). The CellRank pseudotime kernel was initiated with the Palantir pseudotime, and a transition matrix was computed. This, in turn, was used to initiate the GPCCA (*102*) estimator, which allowed the computation of macrostates from the transition matrix. Inhibitory and excitatory neuron trajectory endpoints (plus an additional ChP endpoint in Line 409b2 and FOK4 data) were manually selected from the computed macrostates and, in turn, used to compute the respective fate probabilities for each cell and terminal state. We further used CellRank to compute lineage drivers for each terminal state, correcting for FDR and discarding any drivers where the significance of the driver correlation could not be computed. A driver gene with an FDR below 5% was deemed significant in all downstream analyses. The scipy (*103*) implementation of the *t* test on two related samples of scores was used to compute the significance of the difference between the alignment of consensus DE genes and driver gene directionality between the excitatory and inhibitory neuron lineages across three datasets.

For visualizing gene trends, the knn-smoothing on the expression data, as implemented in the scVelo (*104*) v0.2.5 moments function, was used with 30 principal components and otherwise default parameters. Using these data, gene trends were fitted using the GAMR model (*105*) with seven knots and plotted along Palantir pseudotime.

Processing of public fetal human brain scRNA-seq data

The Cell Ranger–processed count matrices from the recently published first-trimester fetal brain atlas by Braun *et al.* (*48*) were downloaded using the link provided by the authors (https://storage.googleapis.com/linnarsson-lab-human/human_dev_GRCh38-3.0.0.h5ad). The associated organoid age, 10x Chromium chemistry version, and neurotransmitter-transporter (NTT) annotations metadata were obtained from tables S1 and S2 of the publication: https://github.com/linnarsson-lab/developing-human-brain/files/9755355/table_S1.xlsx and https://github.com/linnarsson-lab/developing-human-brain/files/9755350/table_S2.xlsx. Any genes expressed in less than 20 cells were removed. Next, cells with less than 200 genes expressed were removed from the dataset. The total counts of each cell were normalized to 10,000 and $\log(1 + x)$–transformed. Using the CellClass annotation provided by the authors, the dataset was then subset to the clusters Neuron, Neuroblast, Neuronal IPC, and Radial Glia. Using the "Chemistry" annotation, the dataset was further subset to cells collected by the 10x 3′ v2 chemistry. Any cells expressing neither the GABA NTT nor any of the glutamate NTTs were removed from the dataset. Any cells expressing both the GABA NTT and any of the glutamate NTTs were also removed from the dataset. A new metadata column ("NTT_simplified") was created, indicating whether the GABA NTT or any of the glutamate NTTs were expressed in each cell.

Downloaded from https://www.science.org at Helmholtz Zentrum Mnchen - Zentralbibliothek on April 09, 2025

Differential abundance testing

All steps described in this section were applied separately to the data derived from Line 409b2 and Line FOK4. Milopy v0.1.1 (https://github.com/emdann/milopy), the Python implementation of Milo (*45*), was used to test for differential abundance between treated and control cells in 70-day-old organoids. For this, a KNN graph was recomputed in the day 70 data using scanpy with n_neighbors = 30, before applying milopy. Neighborhoods were made and counted using milopy using the "sample" column as replicate information. Differential abundance was computed using milopy with "~ treatment" as the design formula and "treatmentChr-treatmentVeh" as the model contrast. Neighborhoods with an FDR-corrected *P* value of <0.1 were deemed significantly differentially abundant.

scATAC-seq data processing

Count matrices were produced from fastq files using 10x Genomics Cell Ranger ATAC (*106*) v2.0.0 with the reference GRCh38 (Ensembl release 94) (*75*). Unless stated otherwise, all downstream analyses were carried out using the R packages Signac (*107*) v1.9.0 and Seurat (*108*) v4.3.0 on R v4.1.2. The aggregated and filtered peak-barcode matrix from 10x Genomics Cell Ranger ATAC was loaded with Signac together with the associated fragments file and metadata. Any features detected in less than 10 cells and any cells with less than 200 detected features were discarded from the dataset. Gene annotations from the EnsDb.Hsapiens.v86 v2.99.0 (https://bioconductor.org/packages/release/data/annotation/html/EnsDb.Hsapiens.v86.html) were used. Transcription start site (TSS) enrichment, nucleosome signal, and the fraction of reads in peak statistics were computed per cell. AMULET (*109*) was installed from the GitHub main branch (https://github.com/UcarLab/AMULET) at commit 9ce413f and used for detecting and removing doublet cells from the dataset.

For QC, only cells conforming with all the following criteria were kept in the dataset: over 1000 fragments in peak regions, less than 100,000 fragments in peak regions, TSS enrichment score greater than 2.7, TSS enrichment score smaller than 10, over 30% reads in peaks, blacklist ratio smaller than 0.66, and a nucleosome signal ratio below 10. This resulted in 7% of cells being removed and 20,616 remaining cells. TF-IDF normalization (*110*), top feature identification (min.cutoff = "q0"), singular value decomposition, neighbor graph computation, UMAP (*82*) computation, and clustering (*111*) were performed. Gene activities were computed and log-normalized. ChromVar (*112*) activities were computed using the BSgenome.Hsapiens.NCBI.GRCh38 (https://bioconductor.org/packages/release/data/annotation/html/BSgenome.Hsapiens.NCBI.GRCh38.html) genome and motif position frequency matrices from the JASPAR2020 database (https://bioconductor.org/packages/release/data/annotation/html/JASPAR2020.html) (*113*).

Multimodal integration of scRNA-seq and scATAC-seq data

The integration described in this section was carried out individually for the GC-exposed and vehicle data (scRNA-seq and scATAC-seq) from 90-day-old organoids (Veh-Veh and Chr-Veh conditions) using the Python package GLUE (*114*) v0.3.2.

The scATAC-seq data were saved as an h5ad object by exporting to Python using anndata2ri v1.1 (https://github.com/theislab/anndata2ri) automatic conversion. The data were subset for the respective treatment condition and reduced to 101 dimensions using 15 latent semantic indexing iterations, as implemented in GLUE. The first dimension was discarded as it usually correlates strongly with read depth. The resulting representation was used to compute a neighbor graph as implemented in the scanpy (*77*) package (using cosine similarity as a metric), followed by UMAP (*82*) computation also using the scanpy implementation.

The raw scRNA-seq count data were subset to the respective treatment condition and processed using the scanpy package as follows, using default parameters unless stated otherwise: highly variable gene computation (n_top_genes = 2000, flavor = "seurat_v3"), count normalization per cell to the median total counts per cell in the dataset, $\log(1 + x)$ transformation, scaling each feature to unit variance and zero mean, computation of 100 principal components, neighbor graph computation using the cosine similarity metric, and UMAP computation.

A GLUE RNA-anchored guidance graph was computed using the scRNA-seq and scATAC-seq data, and a GLUE model was fitted using a negative binomial probability distribution and highly variable features from both data modalities. Principal components were used as a reduced representation of the scRNA-seq data, while the latent semantic indexing embedding was used for scATAC-seq data. Data from both modalities were passed through the trained GLUE model, and the resulting concatenated representation was used to compute a combined neighbor graph and UMAP representation of the data. A bipartite matching approach (*115*), as implemented in the scim package (https://github.com/ratschlab/scim, master branch, commit 6392e65), was used (get_cost_knn_graph function with knn_k = 15, null_cost_percentile = 99, and capacity_method = "uniform") to match cells from both modalities one by one into "metacells." In cases where no ATAC match was found for an RNA cell, only the RNA information was used. The GLUE latent vector of the cell was calculated as the average latent vector of the matched cells and used for joint neighbor graphs and UMAP computation for data visualization. The Python implementation of MAGIC (*116*) (https://github.com/KrishnaswamyLab/MAGIC) was used to impute gene activities on the matched dataset using $k = 15$ neighbors, decay = 1, thresh = 1×10^{-4}, and four nearest neighbors for kernel bandwidth computation.

GRN inference

The R tool Pando (*117*) v1.0.3 (https://github.com/quadbio/Pando) with R v4.1.2, together with Signac (*107*) v1.9.0 and Seurat (*108*) v4.3.0 for preprocessing, were used to infer GRNs from the integrated multimodal data separately for the two treatment conditions (as in the integration step). The integrated metadata was loaded into a Seurat object, from where the data of the two modalities were preprocessed individually. The scATAC-seq peaks were embedded in low-dimensional space using TF-IDF normalization (*110*), top feature identification (min.cutoff = "q0"), and singular value decomposition. At the same time, the RNA data were log-normalized (normalization.method = "LogNormalize," scale.factor = 10,000), top features were identified (selection.method = "vst," nfeatures = 4000), the data were scaled, and principal components were computed. The GRN was initiated using both data modalities and conserved regions from mammals as included in Pando (phastConsElements20Mammals.UCSC.hg38). Candidate regions were scanned for TF binding sites as provided by Pando (motif2tf data). The resulting data and initialized network were used to infer the GRN (peak_to_gene_method = "Signac," method = "glm") followed by gene module identification (p_thresh = 0.1, nvar_thresh = 2, min_genes_per_module = 1, rsq_thresh = 0.05). ggplot2 (*118*) v3.4.2 and ggraph (https://github.com/thomasp85/ggraph) v2.1.0 were used to generate TF-centered GRN visualizations. As multimodal analyses were

Downloaded from https://www.science.org at Helmholtz Zentrum Mnchen - Zentralbibliothek on April 09, 2025

only carried out in Line 409b2, we applied a stricter false discovery cutoff of 5% to define a DE gene in all DE analyses in this section.

In silico TF perturbation

The steps described in this section were carried out individually for the GC-exposed and vehicle data (scRNA-seq and scATAC-seq) from 90-day-old organoids (Veh-Veh and Chr-Veh conditions). *PBX3* target expression was set to 1.0 normalized counts in the overexpression experiment using the Veh-Veh data. *PBX3* expression was set to 0.0 normalized counts in the KO experiment using the Chr-Veh data.

The base-GRN construction for the in silico perturbation experiment was achieved by first predicting co-accessible peaks from our scATAC-seq data using Cicero (*119*) v1.3.9 (https://github.com/cole-trapnell-lab/cicero-release) with R v4.1.2, followed by TSS annotation and TF binding motif scanning using the CellOracle (*54*) v0.18.0 (https://github.com/morris-lab/CellOracle) motif_analysis module. The GRN was inferred with CellOracle using the base-GRN data, together with raw scRNA-seq counts from 4000 highly variable features (flavor = "seurat_v3"), using the parameters from the CellOracle tutorial [KNN imputation using the number of principal components analysis (PCA) components to obtain an explained variance ratio > 0.002 (but a minimum of 50), $k = 0.025$*number of cells, b_sight = k*8, b_maxl = k*4; GRN computation with $\alpha = 10$]. To prepare GRN perturbation, CellOracle was used to fit the GRN for simulation using cell type–specific TF dictionaries and $\alpha = 10$. The CellOracle GRN perturbation was carried out by adapting the target expression of *PBX3* as described at the beginning of this section and simulating the resulting shift (n_propagation = 3), estimating transition probabilities (n_neighbors = 200, knn_random = True, sampled_fraction = 1), and calculating the resulting embedding shift (sigma_corr = 0.05) on the force-directed graph embedding. To visualize the embedding shifts on a grid, the CellOracle calculate_p_mass function (smooth = 0.8, n_grid = 40, n_neighbors = 200) was used, and the mass filter (min_mass = 0.001) was calculated. The previously computed Palantir pseudotime was used to calculate a differentiation vector field via gradients obtained from transferring the pseudotime data onto the embedding grid with args = {"method": "polynomial," "n_poly":3}. This vector field was used to compute the CellOracle perturbation score by taking its inner product with the previously obtained perturbation vector field. The resulting perturbation score was plotted (vm = 0.015, s = 50) while scaling the simulation vectors by 0.7. For validating the robustness of the results independently of the scATAC-seq data, all computations were repeated as described while using the CellOracle prebuilt promoter base-GRN (hg19_gimmemotifsv5_fpr2).

Statistical testing

Unless stated otherwise, the SciPy (*103*) implementation of the *t* test for the means of two independent samples was used to test for significance throughout the article. Unless stated otherwise, correlation coefficients were computed using the SciPy implementation of the Pearson correlation coefficient and *P* value to test for non-correlation.

Supplementary Materials

The PDF file includes:

Figs. S1 to S6
Legends for tables S1 to S9

Other Supplementary Material for this manuscript includes the following:

Tables S1 to S9

REFERENCES AND NOTES

1. P. Levitt, D. B. Campbell, The genetic and neurobiologic compass points toward common signaling dysfunctions in autism spectrum disorders. *J. Clin. Invest.* **119**, 747–754 (2009).
2. D. H. Geschwind, M. W. State, Gene hunting in autism spectrum disorder: On the path to precision medicine. *Lancet Neurol.* **14**, 1109–1120 (2015).
3. P. F. Sullivan, M. J. Daly, M. O'Donovan, Genetic architectures of psychiatric disorders: The emerging picture and its implications. *Nat. Rev. Genet.* **13**, 537–551 (2012).
4. X. Meng, D. Yao, K. Imaizumi, X. Chen, K. W. Kelley, N. Reis, M. V. Thete, A. Arjun McKinney, S. Kulkarni, G. Panagiotakos, M. C. Bassik, S. P. Paşca, Assembloid CRISPR screens reveal impact of disease genes in human neurodevelopment. *Nature* **622**, 359–366 (2023).
5. M. X. Moreau, Y. Saillour, A. W. Cwetsch, A. Pierani, F. Causeret, Single-cell transcriptomics of the early developing mouse cerebral cortex disentangle the spatial and temporal components of neuronal fate acquisition. *Development* **148**, dev197962 (2021).
6. A. Genovese, M. G. Butler, The autism spectrum: Behavioral, psychiatric and genetic associations. *Genes* **14**, 677 (2023).
7. C. Cheroni, N. Caporale, G. Testa, Autism spectrum disorder at the crossroad between genes and environment: Contributions, convergences, and interactions in ASD developmental pathophysiology. *Mol. Autism.* **11**, 69 (2020).
8. I. Kotsiri, P. Resta, A. Spyrantis, C. Panotopoulos, D. Chaniotis, A. Beloukas, E. Magiorkinis, Viral infections and schizophrenia: A comprehensive review. *Viruses* **15**, 1345 (2023).
9. C. Davies, G. Segre, A. Estradé, J. Radua, A. De Micheli, U. Provenzani, D. Oliver, G. Salazar de Pablo, V. Ramella-Cravaro, M. Besozzi, P. Dazzan, M. Miele, G. Caputo, C. Spallarossa, G. Crossland, A. Ilyas, G. Spada, P. Politi, R. M. Murray, P. McGuire, P. Fusar-Poli, Prenatal and perinatal risk and protective factors for psychosis: A systematic review and meta-analysis. *Lancet Psychiatry* **7**, 399–410 (2020).
10. G. Ursini, G. Punzi, B. W. Langworthy, Q. Chen, K. Xia, E. A. Cornea, B. D. Goldman, M. A. Styner, R. C. Knickmeyer, J. H. Gilmore, D. R. Weinberger, Placental genomic risk scores and early neurodevelopmental outcomes. *Proc. Natl. Acad. Sci. U.S.A.* **118**, e2019789118 (2021).
11. A. C. Krontira, C. Cruceanu, E. B. Binder, Glucocorticoids as mediators of adverse outcomes of prenatal stress. *Trends Neurosci.* **43**, 394–405 (2020).
12. R. C. Painter, T. J. Roseboom, S. R. de Rooij, Long-term effects of prenatal stress and glucocorticoid exposure. *Birth Defects Res. C Embryo Today* **96**, 315–324 (2012).
13. A. M. Graham, J. M. Rasmussen, S. Entringer, E. Ben Ward, M. D. Rudolph, J. H. Gilmore, M. Styner, P. D. Wadhwa, D. A. Fair, C. Buss, Maternal cortisol concentrations during pregnancy and sex-specific associations with neonatal amygdala connectivity and emerging internalizing behaviors. *Biol. Psychiatry* **85**, 172–181 (2019).
14. K. Räikkönen, M. Gissler, E. Kajantie, Maternal antenatal corticosteroid treatment and childhood mental and behavioral disorders-reply. *JAMA* **324**, 1570–1571 (2020).
15. K. Räikkönen, M. Gissler, E. Kajantie, Associations between maternal antenatal corticosteroid treatment and mental and behavioral disorders in children. *JAMA* **323**, 1924–1933 (2020).
16. Y.-H. Lin, C.-H. Lin, M.-C. Lin, Y.-C. Hsu, C.-T. Hsu, Antenatal corticosteroid exposure is associated with childhood mental disorders in late preterm and term infants. *J. Pediatr.* **253**, 245–251.e2 (2023).
17. K. Räikkönen, M. Gissler, T. Tapiainen, E. Kajantie, Associations between maternal antenatal corticosteroid treatment and psychological developmental and neurosensory disorders in children. *JAMA Netw. Open* **5**, e2228518 (2022).
18. K. Ninan, S. K. Liyanage, K. E. Murphy, E. V. Asztalos, S. D. McDonald, Evaluation of long-term outcomes associated with preterm exposure to antenatal corticosteroids: A systematic review and meta-analysis. *JAMA Pediatr.* **176**, e220483 (2022).
19. M. A. Tsiarli, A. Rudine, N. Kendall, M. O. Pratt, R. Krall, E. Thiels, D. B. DeFranco, A. P. Monaghan, Antenatal dexamethasone exposure differentially affects distinct cortical neural progenitor cells and triggers long-term changes in murine cerebral architecture and behavior. *Transl. Psychiatry* **7**, e1153 (2017).
20. E. O. Ohuma, A.-B. Moller, E. Bradley, S. Chakwera, L. Hussain-Alkhateeb, A. Lewin, Y. B. Okwaraji, W. R. Mahanani, E. W. Johansson, T. Lavin, D. E. Fernandez, G. G. Domínguez, A. de Costa, J. A. Cresswell, J. Krasevec, J. E. Lawn, H. Blencowe, J. Requejo, A. C. Moran, National, regional, and global estimates of preterm birth in 2020, with trends from 2010: A systematic analysis. *Lancet* **402**, 1261–1271 (2023).
21. K. Bassil, A. C. Krontira, T. Leroy, A. I. H. Escoto, C. Snijders, C. D. Pernia, R. J. Pasterkamp, L. de Nijs, D. van den Hove, G. Kenis, M. P. Boks, K. Vadodaria, N. P. Daskalakis, E. B. Binder, B. P. F. Rutten, In vitro modeling of the neurobiological effects of glucocorticoids: A review. *Neurobiol. Stress* **23**, 100530 (2023).
22. C. Cruceanu, L. Dony, A. C. Krontira, D. S. Fischer, S. Roeh, R. Di Giaimo, C. Kyrousi, L. Kaspar, J. Arloth, D. Czamara, N. Gerstner, S. Martinelli, S. Wehner, M. S. Breen, M. Koedel, S. Sauer, V. Sportelli, M. Rex-Haffner, S. Cappello, F. J. Theis, E. B. Binder, Cell-type-specific impact of glucocorticoid receptor activation on the developing brain: A cerebral organoid study. *Am. J. Psychiatry* **179**, 375–387 (2022).
23. A. C. Krontira, C. Cruceanu, L. Dony, C. Kyrousi, M.-H. Link, N. Rek, D. Pöhlchen, C. Raimundo, S. Penner-Goeke, A. Schowe, D. Czamara, M. Lahti-Pulkkinen,

Downloaded from https://www.science.org at Helmholtz Zentrum Mnchen - Zentralbibliothek on April 09, 2025

S. Sammallahti, E. Wolford, K. Heinonen, S. Roeh, V. Sportelli, B. Wölfel, M. Ködel, S. Sauer, M. Rex-Haffner, K. Räikkönen, M. Labeur, S. Cappello, E. B. Binder, Human cortical neurogenesis is altered via glucocorticoid-mediated regulation of ZBTB16 expression. *Neuron* **112**, 1426–1443.e11 (2024).
24. A. Jourdon, F. Wu, J. Mariani, D. Capauto, S. Norton, L. Tomasini, A. Amiri, M. Suvakov, J. D. Schreiner, Y. Jang, A. Panda, C. K. Nguyen, E. M. Cummings, G. Han, K. Powell, A. Szekely, J. C. McPartland, K. Pelphrey, K. Chawarska, P. Ventola, A. Abyzov, F. M. Vaccarino, Modeling idiopathic autism in forebrain organoids reveals an imbalance of excitatory cortical neuron subtypes during early neurogenesis. *Nat. Neurosci.* **26**, 1505–1515 (2023).
25. J. Mariani, G. Coppola, P. Zhang, A. Abyzov, L. Provini, L. Tomasini, M. Amenduni, A. Szekely, D. Palejev, M. Wilson, M. Gerstein, E. L. Grigorenko, K. Chawarska, K. A. Pelphrey, J. R. Howe, F. M. Vaccarino, FOXG1-dependent dysregulation of gaba/glutamate neuron differentiation in autism spectrum disorders. *Cell* **162**, 375–390 (2015).
26. X. Qian, Y. Su, C. D. Adam, A. U. Deutschmann, S. R. Pather, E. M. Goldberg, K. Su, S. Li, L. Lu, F. Jacob, P. T. T. Nguyen, S. Huh, A. Hoke, S. E. Swinford-Jackson, Z. Wen, X. Gu, R. C. Pierce, H. Wu, L. A. Briand, H. I. Chen, J. A. Wolf, H. Song, G.-L. Ming, Sliced human cortical organoids for modeling distinct cortical layer formation. *Cell Stem Cell* **26**, 766–781.e9 (2020).
27. D. J. C. Tai, P. Razaz, S. Erdin, D. Gao, J. Wang, X. Nuttle, C. E. de Esch, R. L. Collins, B. B. Currall, K. O'Keefe, N. D. Burt, R. Yadav, L. Wang, K. Mohajeri, T. Aneichyk, A. Ragavendran, A. Stortchevoi, E. Morini, W. Ma, D. Lucente, A. Hastie, R. J. Kelleher, R. H. Perlis, M. E. Talkowski, J. F. Gusella, Tissue- and cell-type-specific molecular and functional signatures of 16p11.2 reciprocal genomic disorder across mouse brain and human neuronal models. *Am. J. Hum. Genet.* **109**, 1789–1813 (2022).
28. T. Sawada, T. E. Chater, Y. Sasagawa, M. Yoshimura, N. Fujimori-Tonou, K. Tanaka, K. J. M. Benjamin, A. C. M. Paquola, J. A. Erwin, Y. Goda, I. Nikaido, T. Kato, Developmental excitation-inhibition imbalance underlying psychoses revealed by single-cell analyses of discordant twins-derived cerebral organoids. *Mol. Psychiatry* **25**, 2695–2711 (2020).
29. C. Li, J. S. Fleck, C. Martins-Costa, T. R. Burkard, J. Themann, M. Stuempflen, A. M. Peer, Á. Vertesy, J. B. Littleboy, C. Esk, U. Elling, G. Kasprian, N. S. Corsini, B. Treutlein, J. A. Knoblich, Single-cell brain organoid screening identifies developmental defects in autism. *Nature* **621**, 373–380 (2023).
30. Á. Vértesy, O. L. Eichmüller, J. Naas, M. Novatchkova, C. Esk, M. Balmaña, S. Ladstaetter, C. Bock, A. von Haeseler, J. A. Knoblich, Gruffi: An algorithm for computational removal of stressed cells from brain organoid transcriptomic datasets. *EMBO J.* **41**, e111118 (2022).
31. M. S. Kukharsky, N. N. Ninkina, H. An, V. Telezhkin, W. Wei, C. R. de Meritens, J. Cooper-Knock, S. Nakagawa, T. Hirose, V. L. Buchman, T. A. Shelkovnikova, Long non-coding RNA Neat1 regulates adaptive behavioural response to stress in mice. *Transl. Psychiatry* **10**, 171 (2020).
32. G. Arun, D. Aggarwal, D. L. Spector, *MALAT1* Long non-coding RNA: Functional implications. *Noncoding RNA* **6**, 22 (2020).
33. S.-A. Ock, J. G. Knott, I. Choi, Involvement of CDKN1A (p21) in cellular senescence in response to heat and irradiation stress during preimplantation development. *Cell Stress Chaperones* **25**, 503–508 (2020).
34. J. Małecki, M. E. Jakobsson, A. Y. Y. Ho, A. Moen, A. C. Rustan, P. Ø. Falnes, Uncovering human METTL12 as a mitochondrial methyltransferase that modulates citrate synthase activity through metabolite-sensitive lysine methylation. *J. Biol. Chem.* **292**, 17950–17962 (2017).
35. H.-O. Rashid, R. K. Yadav, H.-R. Kim, H.-J. Chae, ER stress: Autophagy induction, inhibition and selection. *Autophagy* **11**, 1956–1977 (2015).
36. Z. He, L. Dony, J. S. Fleck, A. Szałata, K. X. Li, I. Slišković, H.-C. Lin, M. Santel, A. Atamian, G. Quadrato, J. Sun, S. P. Paşca, Human Cell Atlas Organoid Biological Network, J. G. Camp, F. J. Theis, B. Treutlein, An integrated transcriptomic cell atlas of human neural organoids. *Nature* **635**, 690–698 (2024).
37. P. M. Pitale, W. Howse, M. Gorbatyuk, Neuronatin protein in health and disease. *J. Cell. Physiol.* **232**, 477–481 (2017).
38. A. Rad, U. Altunoglu, R. Miller, R. Maroofian, K. N. James, A. O. Çağlayan, M. Najafi, V. Stanley, R.-M. Boustany, G. Yeşil, A. Sahebzamani, G. Ercan-Sencicek, K. Saeidi, K. Wu, P. Bauer, Z. Bakey, J. G. Gleeson, N. Hauser, M. Gunel, H. Kayserili, M. Schmidts, MAB21L1 loss of function causes a syndromic neurodevelopmental disorder with distinctive *c* erebellar, *o* cular, cranio *f* acial and enital features (COFG syndrome). *J. Med. Genet.* **56**, 332–339 (2019).
39. K. Runge, R. Mathieu, S. Bugeon, S. Lafi, C. Beurrier, S. Sahu, F. Schaller, A. Loubat, L. Herault, S. Gaillard, E. Pallesi-Pocachard, A. Montheil, A. Bosio, J. A. Rosenfeld, E. Hudson, K. Lindstrom, S. Mercimek-Andrews, L. Jeffries, A. van Haeringen, O. Vanakker, A. Van Hecke, D. Amrom, S. Küry, C. Ratner, R. Jethva, C. Gamble, B. Jacq, L. Fasano, G. Santpere, B. Lorente-Galdos, N. Sestan, A. Gelot, S. Giacuzz, S. Goebbels, A. Represa, C. Cardoso, H. Cremer, A. de Chevigny, Disruption of *NEUROD2* causes a neurodevelopmental syndrome with autistic features via cell-autonomous defects in forebrain glutamatergic neurons. *Mol. Psychiatry* **26**, 6125–6148 (2021).
40. R. Montalbán-Loro, G. Lassi, A. Lozano-Ureña, A. Perez-Villalba, E. Jiménez-Villalba, M. Charalambous, G. Vallortigara, A. E. Horner, L. M. Saksida, T. J. Bussey, J. L. Trejo, V. Tucci, A. C. Ferguson-Smith, S. R. Ferrón, *Dlk1* dosage regulates hippocampal neurogenesis and cognition. *Proc. Natl. Acad. Sci. U.S.A.* **118**, e2015505118 (2021).
41. M. El Amri, U. Fitzgerald, G. Schlosser, MARCKS and MARCKS-like proteins in development and regeneration. *J. Biomed. Sci.* **25**, 43 (2018).
42. B. S. Abrahams, D. E. Arking, D. B. Campbell, H. C. Mefford, E. M. Morrow, L. A. Weiss, I. Menashe, T. Wadkins, S. Banerjee-Basu, A. Packer, SFARI Gene 2.0: A community-driven knowledgebase for the autism spectrum disorders (ASDs). *Mol. Autism* **4**, 36 (2013).
43. S. Kanton, M. J. Boyle, Z. He, M. Santel, A. Weigert, F. Sanchís-Calleja, P. Guijarro, L. Sidow, J. S. Fleck, D. Han, Z. Qian, M. Heide, W. B. Huttner, P. Khaitovich, S. Pääbo, B. Treutlein, J. G. Camp, Organoid single-cell genomic atlas uncovers human-specific features of brain development. *Nature* **574**, 418–422 (2019).
44. M. Lange, V. Bergen, M. Klein, M. Setty, B. Reuter, M. Bakhti, H. Lickert, M. Ansari, J. Schniering, H. B. Schiller, D. Pe'er, F. J. Theis, CellRank for directed single-cell fate mapping. *Nat. Methods* **19**, 159–170 (2022).
45. E. Dann, N. C. Henderson, S. A. Teichmann, M. D. Morgan, J. C. Marioni, Differential abundance testing on single-cell data using k-nearest neighbor graphs. *Nat. Biotechnol.* **40**, 245–253 (2022).
46. J. A. Bagley, D. Reumann, S. Bian, J. Lévi-Strauss, J. A. Knoblich, Fused cerebral organoids model interactions between brain regions. *Nat. Methods* **14**, 743–751 (2017).
47. C. A. Rottkamp, K. J. Lobur, C. L. Wladyka, A. K. Lucky, S. O'Gorman, Pbx3 is required for normal locomotion and dorsal horn development. *Dev. Biol.* **314**, 23–39 (2008).
48. E. Braun, M. Danan-Gotthold, L. E. Borm, K. W. Lee, E. Vinsland, P. Lönnerberg, L. Hu, X. Li, X. He, Ž. Andrusivová, J. Lundeberg, R. A. Barker, E. Arenas, E. Sundström, S. Linnarsson, Comprehensive cell atlas of the first-trimester developing human brain. *Science* **382**, eadf1226 (2023).
49. Y. Shen, C. Zhang, K. Xiao, D. Liu, G. Xie, CELF4 regulates spine formation and depression-like behaviors of mice. *Biochem. Biophys. Res. Commun.* **605**, 39–44 (2022).
50. I. Salamon, Y. Park, T. Miškić, J. Kopić, P. Matteson, N. F. Page, A. Roque, G. W. McAuliffe, J. Favate, M. Garcia-Forn, P. Shah, M. Judaš, J. H. Millonig, I. Kostović, S. De Rubeis, R. P. Hart, Ž. Krsnik, M.-R. Rasin, Celf4 controls mRNA translation underlying synaptic development in the prenatal mammalian neocortex. *Nat. Commun.* **14**, 6025 (2023).
51. R. Barone, M. Fichera, M. De Grandi, M. Battaglia, V. Lo Faro, T. Mattina, R. Rizzo, Familial 18q12.2 deletion supports the role of RNA-binding protein CELF4 in autism spectrum disorders. *Am. J. Med. Genet. A* **173**, 1649–1655 (2017).
52. R. N. Delgado, D. E. Allen, M. G. Keefe, W. R. Mancia Leon, R. S. Ziffra, E. E. Crouch, A. Alvarez-Buylla, T. J. Nowakowski, Individual human cortical progenitors can produce excitatory and inhibitory neurons. *Nature* **601**, 397–403 (2022).
53. S. Blankvoort, L. C. Olsen, C. G. Kentros, Single cell transcriptomic and chromatin profiles suggest layer Vb is the only layer with shared excitatory cell types in the medial and lateral entorhinal cortex. *Front. Neural Circuits* **15**, 806154 (2022).
54. K. Kamimoto, B. Stringa, C. M. Hoffmann, K. Jindal, L. Solnica-Krezel, S. A. Morris, Dissecting cell identity via network inference and in silico gene perturbation. *Nature* **614**, 742–751 (2023).
55. C. Anacker, P. A. Zunszain, L. A. Carvalho, C. M. Pariante, The glucocorticoid receptor: Pivot of depression and of antidepressant treatment? *Psychoneuroendocrinology* **36**, 415–425 (2011).
56. A. Bhaduri, M. G. Andrews, W. Mancia Leon, D. Jung, D. Shin, D. Allen, D. Jung, G. Schmunk, M. Haeussler, J. Salma, A. A. Pollen, T. J. Nowakowski, A. R. Kriegstein, Cell stress in cortical organoids impairs molecular subtype specification. *Nature* **578**, 142–148 (2020).
57. S. L. Giandomenico, S. B. Mierau, G. M. Gibbons, L. M. D. Wenger, L. Masullo, T. Sit, M. Sutcliffe, J. Boulanger, M. Tripodi, E. Derivery, O. Paulsen, A. Lakatos, M. A. Lancaster, Cerebral organoids at the air-liquid interface generate diverse nerve tracts with functional output. *Nat. Neurosci.* **22**, 669–679 (2019).
58. M. A. Lancaster, J. A. Knoblich, Generation of cerebral organoids from human pluripotent stem cells. *Nat. Protoc.* **9**, 2329–2340 (2014).
59. B. F. Bloomer, J. J. Morales, A. R. Bolbecker, D.-J. Kim, W. P. Hetrick, Cerebellar structure and function in autism spectrum disorder. *J. Psychiatr. Brain Sci.* **7**, e220003 (2022).
60. L. Mapelli, T. Soda, E. D'Angelo, F. Prestori, The cerebellar involvement in autism spectrum disorders: From the social brain to mouse models. *Int. J. Mol. Sci.* **23**, 3894 (2022).
61. N. Bast, L. Poustka, C. M. Freitag, The locus coeruleus-norepinephrine system as pacemaker of attention—A developmental mechanism of derailed attentional function in autism spectrum disorder. *Eur. J. Neurosci.* **47**, 115–125 (2018).
62. H. R. Willsey, C. R. T. Exner, Y. Xu, A. Everitt, N. Sun, B. Wang, J. Dea, G. Schmunk, Y. Zaltsman, N. Teerikorpi, A. Kim, A. S. Anderson, D. Shin, M. Seyler, T. J. Nowakowski, R. M. Harland, A. J. Willsey, M. W. State, Parallel in vivo analysis of large-effect autism genes implicates cortical neurogenesis and estrogen in risk and resilience. *Neuron* **109**, 788–804.e8 (2021).
63. N. Caporale, M. Leemans, L. Birgersson, P.-L. Germain, C. Cheroni, G. Borbély, E. Engdahl, C. Lindh, R. B. Bressan, F. Cavallo, N. E. Chorev, G. A. D'Agostino, S. M. Pollard, M. T. Rigoli,

Downloaded from https://www.science.org at Helmholtz Zentrum Mnchen - Zentralbibliothek on April 09, 2025

E. Tenderini, A. L. Tobon, S. Trattaro, F. Troglio, M. Zanella, Å. Bergman, P. Damdimopoulou, M. Jönsson, W. Kiess, E. Kitraki, H. Kiviranta, E. Nånberg, M. Öberg, P. Rantakokko, C. Rudén, O. Söder, C.-G. Bornehag, B. Demeneix, J.-B. Fini, C. Gennings, J. Rüegg, J. Sturve, G. Testa, From cohorts to molecules: Adverse impacts of endocrine disrupting mixtures. *Science* **375**, eabe8244 (2022).

64. J. W. Brunner, H. C. A. Lammertse, A. A. van Berkel, F. Koopmans, K. W. Li, A. B. Smit, R. F. Toonen, M. Verhage, S. van der Sluis, Power and optimal study design in iPSC-based brain disease modelling. *Mol. Psychiatry* **28**, 1545–1556 (2023).
65. C. Bizzarri, M. Cappa, Ontogeny of hypothalamus-pituitary gonadal axis and minipuberty: An ongoing debate? *Front. Endocrinol.* **11**, 187 (2020).
66. A. Pavlinek, D. Adhya, A. Tsompanidis, V. Warrier, APEX Consortium, A. C. Vernon, M. Lancaster, J. Mill, D. P. Srivastava, S. Baron-Cohen, Using organoids to model sex differences in the human brain. *Biol. Psychiatry Glob. Open Sci.* **4**, 100343 (2024).
67. I. Kelava, I. Chiaradia, L. Pellegrini, A. T. Kalinka, M. A. Lancaster, Androgens increase excitatory neurogenic potential in human brain organoids. *Nature* **602**, 112–116 (2022).
68. S. P. Paşca, P. Arlotta, H. S. Bateup, J. G. Camp, S. Cappello, F. H. Gage, J. A. Knoblich, A. R. Kriegstein, M. A. Lancaster, G.-L. Ming, A. R. Muotri, I.-H. Park, O. Reiner, H. Song, L. Studer, S. Temple, G. Testa, B. Treutlein, F. M. Vaccarino, A nomenclature consensus for nervous system organoids and assembloids. *Nature* **609**, 907–910 (2022).
69. M. Koyanagi-Aoi, M. Ohnuki, K. Takahashi, K. Okita, H. Noma, Y. Sawamura, I. Teramoto, M. Narita, Y. Sato, T. Ichisaka, N. Amano, A. Watanabe, A. Morizane, Y. Yamada, T. Sato, J. Takahashi, S. Yamanaka, Differentiation-defective phenotypes revealed by large-scale analyses of human pluripotent stem cells. *Proc. Natl. Acad. Sci. U.S.A.* **110**, 20569–20574 (2013).
70. K. Okita, Y. Matsumura, Y. Sato, A. Okada, A. Morizane, S. Okamoto, H. Hong, M. Nakagawa, K. Tanabe, K.-i. Tezuka, T. Shibata, T. Kunisada, M. Takahashi, J. Takahashi, H. Saji, S. Yamanaka, A more efficient method to generate integration-free human iPS cells. *Nat. Methods* **8**, 409–412 (2011).
71. T. M. Brückl, V. I. Spoormaker, P. G. Sämann, A.-K. Brem, L. Henco, D. Czamara, I. Elbau, N. C. Grandi, L. Jollans, A. Kühnel, L. Leuchs, D. Pöhlchen, M. Schneider, A. Tontsch, M. E. Keck, L. Schilbach, M. Czisch, S. Lucae, A. Erhardt, E. B. Binder, The biological classification of mental disorders (BeCOME) study: A protocol for an observational deep-phenotyping study for the identification of biological subtypes. *BMC Psychiatry* **20**, 213 (2020).
72. S. Riesenberg, T. Maricic, Targeting repair pathways with small molecules increases precise genome editing in pluripotent stem cells. *Nat. Commun.* **9**, 2164 (2018).
73. N. Provençal, J. Arloth, A. Cattaneo, C. Anacker, N. Cattane, T. Wiechmann, S. Röh, M. Ködel, T. Klengel, D. Czamara, N. S. Müller, J. Lahti, PREDO team, K. Räikkönen, C. M. Pariante, E. B. Binder, Glucocorticoid exposure during hippocampal neurogenesis primes future stress response by inducing changes in DNA methylation. *Proc. Natl. Acad. Sci. U.S.A.* **117**, 23280–23285 (2020).
74. G. X. Y. Zheng, J. M. Terry, P. Belgrader, P. Ryvkin, Z. W. Bent, R. Wilson, S. B. Ziraldo, T. D. Wheeler, G. P. McDermott, J. Zhu, M. T. Gregory, J. Shuga, L. Montesclaros, J. G. Underwood, D. A. Masquelier, S. Y. Nishimura, M. Schnall-Levin, P. W. Wyatt, C. M. Hindson, R. Bharadwaj, A. Wong, K. D. Ness, L. W. Beppu, H. J. Deeg, C. McFarland, K. R. Loeb, W. J. Valente, N. G. Ericson, E. A. Stevens, J. P. Radich, T. S. Mikkelsen, B. J. Hindson, J. H. Bielas, Massively parallel digital transcriptional profiling of single cells. *Nat. Commun.* **8**, 14049 (2017).
75. F. Cunningham, P. Achuthan, W. Akanni, J. Allen, M. R. Amode, I. M. Armean, R. Bennett, J. Bhai, K. Billis, S. Boddu, C. Cummins, C. Davidson, K. J. Dodiya, A. Gall, C. G. Girón, L. Gil, T. Grego, L. Haggerty, E. Haskell, T. Hourlier, O. G. Izuogu, S. H. Janacek, T. Juettemann, M. Kay, M. R. Laird, I. Lavidas, Z. Liu, J. E. Loveland, J. C. Marugán, T. Maurel, A. C. McMahon, B. Moore, J. Morales, J. M. Mudge, M. Nuhn, D. Ogeh, A. Parker, A. Parton, M. Patricio, A. I. Abdul Salam, B. M. Schmitt, H. Schuilenburg, D. Sheppard, H. Sparrow, E. Stapleton, M. Szuba, K. Taylor, G. Threadgold, A. Thormann, A. Vullo, B. Walts, A. Winterbottom, A. Zadissa, M. Chakiachvili, A. Frankish, S. E. Hunt, M. Kostadima, N. Langridge, F. J. Martin, M. Muffato, E. Perry, M. Ruffier, D. M. Staines, S. J. Trevanion, B. L. Aken, A. D. Yates, D. R. Zerbino, P. Flicek, Ensembl 2019. *Nucleic Acids Res.* **47**, D745–D751 (2019).
76. I. Virshup, D. Bredikhin, L. Heumos, G. Palla, G. Sturm, A. Gayoso, I. Kats, M. Koutrouli, Scverse Community, B. Berger, D. Pe'er, A. Regev, S. A. Teichmann, F. Finotello, F. A. Wolf, N. Yosef, O. Stegle, F. J. Theis, The scverse project provides a computational ecosystem for single-cell omics data analysis. *Nat. Biotechnol.* **41**, 604–606 (2023).
77. F. A. Wolf, P. Angerer, F. J. Theis, SCANPY: Large-scale single-cell gene expression data analysis. *Genome Biol.* **19**, 15 (2018).
78. I. Virshup, S. Rybakov, F. J. Theis, P. Angerer, F. A. Wolf, anndata: Access and store annotated data matrices. *J. Open Source Softw.* **9**, 4371 (2024).
79. V. D. Blondel, J.-L. Guillaume, R. Lambiotte, E. Lefebvre, Fast unfolding of communities in large networks. *J. Stat. Mech.* **2008**, P10008 (2008).
80. A. T. L. Lun, K. Bach, J. C. Marioni, Pooling across cells to normalize single-cell RNA sequencing data with many zero counts. *Genome Biol.* **17**, 75 (2016).
81. F. Pedregosa, G. Varoquaux, A. Gramfort, V. Michel, B. Thirion, O. Grisel, M. Blondel, P. Prettenhofer, R. Weiss, V. Dubourg, J. Vanderplas, A. Passos, D. Cournapeau, M. Brucher, M. Perrot, É. Duchesnay, Scikit-learn: Machine learning in python. *J. Mach. Learn. Res.* **12**, 2825–2830 (2011).
82. L. McInnes, J. Healy, J. Melville, UMAP: Uniform manifold approximation and projection for dimension reduction. arXiv:1802.03426 [stat.ML] (2018).
83. M. Jacomy, T. Venturini, S. Heymann, M. Bastian, ForceAtlas2, a continuous graph layout algorithm for handy network visualization designed for the Gephi software. *PLOS ONE* **9**, e98679 (2014).
84. F. A. Wolf, F. K. Hamey, M. Plass, J. Solana, J. S. Dahlin, B. Göttgens, N. Rajewsky, L. Simon, F. J. Theis, PAGA: Graph abstraction reconciles clustering with trajectory inference through a topology preserving map of single cells. *Genome Biol.* **20**, 59 (2019).
85. M. Ashburner, C. A. Ball, J. A. Blake, D. Botstein, H. Butler, J. M. Cherry, A. P. Davis, K. Dolinski, S. S. Dwight, J. T. Eppig, M. A. Harris, D. P. Hill, L. Issel-Tarver, A. Kasarskis, S. Lewis, J. C. Matese, J. E. Richardson, M. Ringwald, G. M. Rubin, G. Sherlock, Gene ontology: Tool for the unification of biology. The gene ontology consortium. *Nat. Genet.* **25**, 25–29 (2000).
86. Gene Ontology Consortium, S. A. Aleksander, J. Balhoff, S. Carbon, J. M. Cherry, H. J. Drabkin, D. Ebert, M. Feuermann, P. Gaudet, N. L. Harris, D. P. Hill, R. Lee, H. Mi, S. Moxon, C. J. Mungall, A. Muruganugan, T. Mushayahama, P. W. Sternberg, P. D. Thomas, K. Van Auken, J. Ramsey, D. A. Siegele, R. L. Chisholm, P. Fey, M. C. Aspromonte, M. V. Nugnes, F. Quaglia, S. Tosatto, M. Giglio, S. Nadendla, G. Antonazzo, H. Attrill, G. Dos Santos, S. Marygold, V. Strelets, C. J. Tabone, J. Thurmond, P. Zhou, S. H. Ahmed, P. Asanitthong, D. L. Buitrago, M. N. Erdol, M. C. Gage, M. A. Kadhum, K. Y. C. Li, M. Long, A. Michalak, A. Pesala, A. Pritazahra, S. C. C. Saverimuttu, R. Su, K. E. Thurlow, R. C. Lovering, C. Logie, S. Oliferenko, J. Blake, K. Christie, L. Corbani, M. E. Dolan, H. J. Drabkin, D. P. Hill, L. Ni, D. Sitnikov, C. Smith, A. Cuzick, J. Seager, L. Cooper, J. Elser, P. Jaiswal, P. Gupta, P. Jaiswal, S. Naithani, M. Lera-Ramirez, K. Rutherford, V. Wood, J. L. De Pons, M. R. Dwinell, G. T. Hayman, M. L. Kaldunski, A. E. Kwitek, S. J. F. Laulederkind, M. A. Tutaj, M. Vedi, S.-J. Wang, P. D'Eustachio, L. Aimo, K. Axelsen, A. Bridge, N. Hyka-Nouspikel, A. Morgat, S. A. Aleksander, J. M. Cherry, S. R. Engel, K. Karra, S. R. Miyasato, R. S. Nash, M. S. Skrzypek, S. Weng, E. D. Wong, E. Bakker, T. Z. Berardini, L. Reiser, A. Auchincloss, K. Axelsen, G. Argoud-Puy, M.-C. Blatter, E. Boutet, L. Breuza, A. Bridge, C. Casals-Casas, E. Coudert, A. Estreicher, M. L. Famiglietti, M. Feuermann, A. Gos, N. Gruaz-Gumowski, C. Hulo, N. Hyka-Nouspikel, F. Jungo, P. Le Mercier, D. Lieberherr, P. Masson, A. Morgat, I. Pedruzzi, L. Pourcel, S. Poux, C. Rivoire, S. Sundaram, A. Bateman, E. Bowler-Barnett, H. Bye-A-Jee, P. Denny, A. Ignatchenko, R. Ishtiaq, A. Lock, Y. Lussi, M. Magrane, M. J. Martin, S. Orchard, P. Raposo, E. Speretta, N. Tyagi, K. Warner, R. Zaru, A. D. Diehl, R. Lee, J. Chan, S. Diamantakis, D. Raciti, M. Zarowiecki, M. Fisher, C. James-Zorn, V. Ponferrada, A. Zorn, S. Ramachandran, L. Ruzicka, M. Westerfield, The gene ontology knowledgebase in 2023. *Genetics* **224**, iyad031 (2023).
87. L. Pellegrini, C. Bonfio, J. Chadwick, F. Begum, M. Skehel, M. A. Lancaster, Human CNS barrier-forming organoids with cerebrospinal fluid production. *Science* **369**, eaaz5626 (2020).
88. C. De Donno, S. Hediyeh-Zadeh, A. A. Moinfar, M. Wagenstetter, L. Zappia, M. Lotfollahi, F. J. Theis, Population-level integration of single-cell datasets enables multi-scale analysis across samples. *Nat. Methods* **20**, 1683–1692 (2023).
89. M. Lotfollahi, M. Naghipourfar, M. D. Luecken, M. Khajavi, M. Büttner, M. Wagenstetter, Ž. Avsec, A. Gayoso, N. Yosef, M. Interlandi, S. Rybakov, A. V. Misharin, F. J. Theis, Mapping single-cell data to reference atlases by transfer learning. *Nat. Biotechnol.* **40**, 121–130 (2022).
90. G. Finak, A. McDavid, M. Yajima, J. Deng, V. Gersuk, A. K. Shalek, C. K. Slichter, H. W. Miller, M. J. McElrath, M. Prlic, P. S. Linsley, R. Gottardo, MAST: A flexible statistical framework for assessing transcriptional changes and characterizing heterogeneity in single-cell RNA sequencing data. *Genome Biol.* **16**, 278 (2015).
91. A. Lex, N. Gehlenborg, H. Strobelt, R. Vuillemot, H. Pfister, UpSet: Visualization of intersecting sets. *IEEE Trans. Vis. Comput. Graph.* **20**, 1983–1992 (2014).
92. E. Y. Chen, C. M. Tan, Y. Kou, Q. Duan, Z. Wang, G. V. Meirelles, N. R. Clark, A. Ma'ayan, Enrichr: Interactive and collaborative HTML5 gene list enrichment analysis tool. *BMC Bioinformatics* **14**, 128 (2013).
93. M. V. Kuleshov, M. R. Jones, A. D. Rouillard, N. F. Fernandez, Q. Duan, Z. Wang, S. Koplev, S. L. Jenkins, K. M. Jagodnik, A. Lachmann, M. G. McDermott, C. D. Monteiro, G. W. Gundersen, A. Ma'ayan, Enrichr: A comprehensive gene set enrichment analysis web server 2016 update. *Nucleic Acids Res.* **44**, W90–W97 (2016).
94. Z. Fang, X. Liu, G. Peltz, GSEApy: A comprehensive package for performing gene set enrichment analysis in Python. *Bioinformatics* **39**, btac757 (2023).
95. S. Müller-Dott, E. Tsirvouli, M. Vazquez, R. O. Ramirez Flores, P. Badia-I-Mompel, R. Fallegger, D. Türei, A. Lægreid, J. Saez-Rodriguez, Expanding the coverage of regulons from high-confidence prior knowledge for accurate estimation of transcription factor activities. *Nucleic Acids Res.* **51**, 10934–10949 (2023).
96. P. Badia-i-Mompel, J. Vélez Santiago, J. Braunger, C. Geiss, D. Dimitrov, S. Müller-Dott, P. Taus, A. Dugourd, C. H. Holland, R. O. Ramirez Flores, J. Saez-Rodriguez, decoupleR:

Downloaded from https://www.science.org at Helmholtz Zentrum Mnchen - Zentralbibliothek on April 09, 2025

Ensemble of computational methods to infer biological activities from omics data. *Bioinform. Adv.* **2**, vbac016 (2022).
97. M. J. M. F. Reijnders, R. M. Waterhouse, Summary visualizations of gene ontology terms with GO-figure! *Front. Bioinform.* **1**, 638255 (2021).
98. K. Polański, M. D. Young, Z. Miao, K. B. Meyer, S. A. Teichmann, J.-E. Park, BBKNN: Fast batch alignment of single cell transcriptomes. *Bioinformatics* **36**, 964–965 (2020).
99. M. Setty, V. Kiseliovas, J. Levine, A. Gayoso, L. Mazutis, D. Pe'er, Characterization of cell fate probabilities in single-cell data with Palantir. *Nat. Biotechnol.* **37**, 451–460 (2019).
100. L. van der Maaten, G. Hinton, Visualizing data using t-SNE. *J. Mach. Learn. Res.* **9**, 2579–2605 (2008).
101. P. Weiler, M. Lange, M. Klein, D. Pe'er, F. Theis, CellRank 2: Unified fate mapping in multiview single-cell data. *Nat. Methods* **21**, 1196–1205 (2024).
102. B. Reuter, K. Fackeldey, M. Weber, Generalized Markov modeling of nonreversible molecular kinetics. *J. Chem. Phys.* **150**, 174103 (2019).
103. P. Virtanen, R. Gommers, T. E. Oliphant, M. Haberland, T. Reddy, D. Cournapeau, E. Burovski, P. Peterson, W. Weckesser, J. Bright, S. J. van der Walt, M. Brett, J. Wilson, K. J. Millman, N. Mayorov, A. R. J. Nelson, E. Jones, R. Kern, E. Larson, C. J. Carey, İ. Polat, Y. Feng, E. W. Moore, J. VanderPlas, D. Laxalde, J. Perktold, R. Cimrman, I. Henriksen, E. A. Quintero, C. R. Harris, A. M. Archibald, A. H. Ribeiro, F. Pedregosa, P. van Mulbregt, SciPy 1.0 Contributors, SciPy 1.0: Fundamental algorithms for scientific computing in Python. *Nat. Methods* **17**, 261–272 (2020).
104. V. Bergen, M. Lange, S. Peidli, F. A. Wolf, F. J. Theis, Generalizing RNA velocity to transient cell states through dynamical modeling. *Nat. Biotechnol.* **38**, 1408–1414 (2020).
105. S. N. Wood, Fast stable restricted maximum likelihood and marginal likelihood estimation of semiparametric generalized linear models. *J. R. Stat. Soc. Ser. B Stat. Methodol.* **73**, 3–36 (2011).
106. A. T. Satpathy, J. M. Granja, K. E. Yost, Y. Qi, F. Meschi, G. P. McDermott, B. N. Olsen, M. R. Mumbach, S. E. Pierce, M. R. Corces, P. Shah, J. C. Bell, D. Jhutty, C. M. Nemec, J. Wang, L. Wang, Y. Yin, P. G. Giresi, A. L. S. Chang, G. X. Y. Zheng, W. J. Greenleaf, H. Y. Chang, Massively parallel single-cell chromatin landscapes of human immune cell development and intratumoral T cell exhaustion. *Nat. Biotechnol.* **37**, 925–936 (2019).
107. T. Stuart, A. Srivastava, S. Madad, C. A. Lareau, R. Satija, Single-cell chromatin state analysis with Signac. *Nat. Methods* **18**, 1333–1341 (2021).
108. Y. Hao, S. Hao, E. Andersen-Nissen, W. M. Mauck III, S. Zheng, A. Butler, M. J. Lee, A. J. Wilk, C. Darby, M. Zager, P. Hoffman, M. Stoeckius, E. Papalexi, E. P. Mimitou, J. Jain, A. Srivastava, T. Stuart, L. M. Fleming, B. Yeung, A. J. Rogers, J. M. McElrath, C. A. Blish, R. Gottardo, P. Smibert, R. Satija, Integrated analysis of multimodal single-cell data. *Cell* **184**, 3573–3587.e29 (2021).
109. A. Thibodeau, A. Eroglu, C. S. McGinnis, N. Lawlor, D. Nehar-Belaid, R. Kursawe, R. Marches, D. N. Conrad, G. A. Kuchel, Z. J. Gartner, J. Banchereau, M. L. Stitzel, A. E. Cicek, D. Ucar, AMULET: A novel read count-based method for effective multiplet detection from single nucleus ATAC-seq data. *Genome Biol.* **22**, 252 (2021).
110. T. Stuart, A. Butler, P. Hoffman, C. Hafemeister, E. Papalexi, W. M. Mauck III, Y. Hao, M. Stoeckius, P. Smibert, R. Satija, Comprehensive integration of single-cell data. *Cell* **177**, 1888–1902.e21 (2019).
111. L. Waltman, N. J. van Eck, A smart local moving algorithm for large-scale modularity-based community detection. arXiv:1308.6604 [physics.soc-ph] (2013).
112. A. N. Schep, B. Wu, J. D. Buenrostro, W. J. Greenleaf, chromVAR: Inferring transcription-factor-associated accessibility from single-cell epigenomic data. *Nat. Methods* **14**, 975–978 (2017).
113. O. Fornes, J. A. Castro-Mondragon, A. Khan, R. van der Lee, X. Zhang, P. A. Richmond, B. P. Modi, S. Correard, M. Gheorghe, D. Baranašić, W. Santana-Garcia, G. Tan, J. Chèneby, B. Ballester, F. Parcy, A. Sandelin, B. Lenhard, W. W. Wasserman, A. Mathelier, JASPAR 2020: Update of the open-access database of transcription factor binding profiles. *Nucleic Acids Res.* **48**, D87–D92 (2020).
114. Z.-J. Cao, G. Gao, Multi-omics single-cell data integration and regulatory inference with graph-linked embedding. *Nat. Biotechnol.* **40**, 1458–1466 (2022).
115. S. G. Stark, J. Ficek, F. Locatello, X. Bonilla, S. Chevrier, F. Singer, Tumor Profiler Consortium, G. Rätsch, K.-V. Lehmann, SCIM: Universal single-cell matching with unpaired feature sets. *Bioinformatics* **36**, i919–i927 (2020).
116. D. van Dijk, R. Sharma, J. Nainys, K. Yim, P. Kathail, A. J. Carr, C. Burdziak, K. R. Moon, C. L. Chaffer, D. Pattabiraman, B. Bierie, L. Mazutis, G. Wolf, S. Krishnaswamy, D. Pe'er, Recovering gene interactions from single-cell data using data diffusion. *Cell* **174**, 716–729.e27 (2018).
117. J. S. Fleck, S. M. J. Jansen, D. Wollny, F. Zenk, M. Seimiya, A. Jain, R. Okamoto, M. Santel, Z. He, J. G. Camp, B. Treutlein, Inferring and perturbing cell fate regulomes in human brain organoids. *Nature* **621**, 365–372 (2023).
118. H. Wickham, *ggplot2: Elegant Graphics for Data Analysis* (Springer, 2016).
119. H. A. Pliner, J. S. Packer, J. L. McFaline-Figueroa, D. A. Cusanovich, R. M. Daza, D. Aghamirzaie, S. Srivatsan, X. Qiu, D. Jackson, A. Minkina, A. C. Adey, F. J. Steemers, J. Shendure, C. Trapnell, Cicero predicts cis-regulatory DNA interactions from single-cell chromatin accessibility data. *Mol. Cell* **71**, 858–871.e8 (2018).

Acknowledgments: We thank I. Slišković for input on time-resolved gene expression trends from the HNOCA. We thank Z. He for helpful discussions on neural cell identity in organoids and associated marker genes. We thank M. Lange for their valuable input on lineage analysis with CellRank. We thank the sequencing core facility at the Max Planck Institute for Molecular Genetics (Berlin, Germany) for their high-throughput sequencing services. We thank the Core Facility Genomics (CF-GEN) at Helmholtz Munich (Germany) for their services in processing our scRNA-seq and scATAC-seq data with Cell Ranger. **Funding:** This work was supported by the BMBF-funded de.NBI Cloud within the German Network for Bioinformatics Infrastructure (de.NBI) (031A532B, 031A533A, 031A533B, 031A534A, 031A535A, 031A537A, 031A537B, 031A537C, 031A537D, 031A538A) (to L.D.). L.D. acknowledges support from the Joachim Herz Foundation. C.C. acknowledges support from the Sven and Ebba-Cristina Foundation, Jeanssons Stiftelser, and StratNeuro at KI. E.B.B. acknowledges support for this study from a Distinguished Investigator grant from the Brain & Behavior Research Foundation (BBRF) and funding from the Hope for Depression Research Foundation within the Depression Task Force. The study was funded by the Federal Ministry of Education and Research [Bundesministerium für Bildung und Forschung (BMBF)] and the Ministry of Bavaria within the initial phase of the German Center for Mental Health (DZPG) Munich site (grants: 01EE2303D and 01EE2303E).
Author contributions: Conceptualization: L.D., A.C.K., L.K., F.J.T., C.C., and E.B.B. Data curation: L.D. and C.C. Formal analysis: L.D., I.S.D., T.S., F.B., and C.C. Funding acquisition: F.J.T., C.C., and E.B.B. Investigation: L.D., A.C.K., R.A., I.S.D., M.G., T.S., V.S., C.R., M.K., and C.C. Methodology: L.D., A.C.K., R.A., M.L., S.C., F.J.T., C.C., and E.B.B. Project administration: F.J.T., C.C., and E.B.B. Software: L.D. Resources: L.D., M.K., M.L., F.J.T., C.C., and E.B.B. Supervision: S.C., F.J.T., C.C., and E.B.B. Validation: L.D., R.A., I.S.D., V.S., C.R., and C.C. Visualization: L.D., I.S.D., M.G., F.B., and C.C. Writing—original draft: L.D., C.C., and E.B.B. Writing—review and editing: L.D., A.C.K., L.K., I.S.D., M.L., F.J.T., C.C., and E.B.B. **Competing interests:** F.J.T. consults for Immunai Inc., Singularity Bio B.V., CytoReason Ltd., and Cellarity, and has ownership interest in Dermagnostix GmbH and Cellarity. All other authors declare that they have no competing interests. **Data and materials availability:** All data needed to evaluate the conclusions in the paper are present in the paper, Supplementary Materials, and/or the locations specified in this section. Processed count matrices in h5ad format (scRNA-seq and scATAC-seq) with associated metadata, as well as all analysis code, are available from Zenodo (DOI: 10.5281/zenodo.10391945; https://doi.org/10.5281/zenodo.10391945). Raw scRNA-seq data (including filtered count matrices) are available from the Gene Expression Omnibus repository: GSE252522 (https://www.ncbi.nlm.nih.gov/geo/query/acc.cgi?acc=GSE252522) (scRNA-seq Veh, Chr, Chr-Veh, and Chr-Acu conditions), GSE189534 (https://www.ncbi.nlm.nih.gov/geo/query/acc.cgi?acc=GSE189534) (scRNA-seq Veh-Veh and Veh-Acu conditions; Line FOK4 = Line2; Line 409b2 = Line3; Veh-Veh = Veh, Veh-Acu = Dex). Raw scATAC-seq data (including filtered count matrices) are available from the Gene Expression Omnibus repository: GSE252523 (https://www.ncbi.nlm.nih.gov/geo/query/acc.cgi?acc=GSE252523). The MTA for the use of the 409b2 line was obtained from the Riken institute according to their standard policies and approval by the Ludwig Maximilian University of Munich ethics committee. The in-house reprogrammed FOK4 line can be provided by the corresponding authors pending scientific review and a completed MTA. Requests should be submitted to E.B.B.

Submitted 7 January 2024
Accepted 15 January 2025
Published 14 February 2025
10.1126/sciadv.adn8631

Downloaded from https://www.science.org at Helmholtz Zentrum Mnchen - Zentralbibliothek on April 09, 2025